J. Fluid Mech. (1993), *vol.* 253, *pp.* 173–209

Instabilities of two-dimensional inviscid compressible vortices

By W. M. CHAN[1]†, K. SHARIFF[2] AND T. H. PULLIAM[2]

[1] Department of Mechanical Engineering, Stanford University, Stanford, CA 94305, USA

[2] NASA Ames Research Center, Moffett Field, CA 94035, USA

(Received 27 April 1992 and in revised form 6 February 1993)

The linear stability and subsequent nonlinear evolution and acoustic radiation of a planar inviscid compressible vortex is examined. Linear-stability analysis shows that vortices with smoother vorticity profiles than the Rankine vortex considered by Broadbent & Moore (1979) are also unstable. However, only neutrally stable waves are found for a Gaussian vorticity profile. The effects of entropy gradient are investigated and for the particular entropy profile chosen, positive average entropy gradient in the vortex core is destabilizing while the opposite is true for negative average entropy gradient.

The linear initial-value problem is studied by finite-difference methods. It is found that these methods are capable of accurately computing the frequencies and weak growth rates of the normal modes. When the initial condition consists of random perturbations, the long-time behaviour is found to correspond to the most unstable normal mode in all cases. In particular, the Gaussian vortex has no algebraically growing modes. This procedure also reveals the existence of weakly decaying and neutrally stable waves rotating in the direction opposite to the vortex core, which were not observed previously.

The nonlinear development of an elliptic-mode perturbation is studied by numerical solution of the Euler equations. The vortex elongates and forms shocklets; eventually, the core splits into two corotating vortices. The individual vortices then gradually move away from each other while their rate of rotation about their mid-point slowly decreases. The acoustic flux reaches a maximum at the time of fission and decreases as the vortices move apart.

1. Introduction

Relatively little is known about the structure and behaviour of vortices when compressibility effects become important. This has recently prompted a number of investigations of isolated compressible vortices. For example Mandella (1987) measured profiles of velocity, pressure, etc. in a vortex (assumed to be axisymmetric) generated by a shock wave exiting a shock tube. Colonius, Lele & Moin (1991) used analysis and numerical computation to study the time-dependent effects of viscous spreading and heat conduction on an axisymmetric vortex.

The focus of the present work is the behaviour of two-dimensional perturbations superimposed on an axisymmetric vortex with the motion assumed to be non-dissipative. For instance, an elliptic perturbation is provided by a shock wave passing over an axisymmetric vortex in the laboratory (Dosanjh & Weeks 1965).

---

† Present address: NASA Ames Research Center, MS T045-2, Moffett Field, CA 94035, USA.

Two mechanisms are known for two-dimensional instabilities of compressible vortices. (Incompressible mechanisms such as rollup of an annular vorticity concentration can also occur, modified by the effects of compressibility. However, we do not consider such vorticity distributions here.) The first mechanism, which will not be considered in detail here, is that if radially displaced fluid parcels change density adiabatically, then the centrifugal force induces a buoyancy-like effect for a non-homentropic basic state. There are a number of stability conditions (see the appendix in Hultgren 1988 for a synopsis) in which this effect is represented. These stability conditions can be limited to the homentropic case and one sees (from Hultgren's equation (A 1)) that the sufficient condition for stability to two-dimensional disturbances is violated in an irrotational region or for a Gaussian vorticity at sufficiently large radius. Similarly, Ripa (1987) obtained sufficient conditions for stability of shallow-water vortices which are analogous to homentropic gasdynamic vortices with specific heat ratio $\gamma = 2$. For a uniform-vorticity core surrounded by irrotational flow (Rankine vortex), it is possible to prove stability when the Mach number and the radius are below certain values but the conditions can always be violated for a given Mach number at sufficiently large radii. This implies stability for a confined vortex with sufficiently small ratio of container to vortex radius.

The second mechanism for instability, which is the main concern of this work, is related directly to acoustics. Over a century ago, Kelvin (1880) showed that an incompressible unbounded Rankine vortex could support a spectrum of neutrally stable modes. With the addition of slight compressibility (i.e. at small Mach numbers) these modes radiate sound (Broadbent 1976), the elliptic mode being the most efficient. One might be tempted to think that acoustic loss of energy from the system should cause perturbations to decay. However, the linear stability analysis of Broadbent & Moore (1979), valid for arbitrary Mach number, showed that the modes are in fact destabilized by compressibility. One simple way to understand the instability, due to Kop'ev & Leont'ev (1983, 1988), is to recognize that the incompressible Rankine vortex with uniform density maximizes energy relative to neighbouring isovortical states: the more the vortex is perturbed the less its energy. The perturbations are said to have 'negative disturbance energy'. Hence perturbations cannot grow or decay without an external sink or source of energy and this accounts for neutral stability of the vortex (Hayashi & Young 1987). However, with the addition of slight compressibility, loss of energy by acoustic radiation allows perturbations to grow. The idea has been used by Zeitlin (1991) to predict the exact nonlinear growth, at low Mach number, in the vortex shapes of a class of exact solutions to the Euler equations having cycloidal particle paths. In these solutions, the vorticity need not be uniform and deviation from circular symmetry can be large. Because the rate of energy loss by acoustic radiation is an inefficient process, growth rates for this instability mechanism are necessarily small compared to inertial timescales.

A very similar instability mechanism has been studied in geophysical contexts (Hayashi & Young 1987) where a mode with negative disturbance energy can resonate and transfer energy to a mode of positive disturbance energy so that both grow. For the compressible vortex, this suggests that instability can result not only from acoustic radiation but also from transfer of energy to a confined acoustic component, for instance, for a vortex surrounded by a rigid enclosure. Sozou (1969*a*, *b*) and Sozou & Swithenbank (1969) have reported on the existence of various types of neutral modes for a Rankine vortex in a cylindrical enclosure. Transfer of energy to an acoustic component and hence instability may become possible at larger cylinder radii than considered in their paper.

Broadbent (1984) considered the linear stability of a smoother two-core vortex consisting of an inner core with solid-body rotation, an outer core with a power law circumferential velocity and potential flow in the unbounded region outside the vortex. For the same Mach number at the vortical core boundary M_v, the two-core vortex is slightly more unstable than the Rankine vortex. If the two-core vortex is compared with a Rankine vortex of the same circulation, then the growth rate of the two-core vortex increases more rapidly with M_v.

Broadbent (1984) and Sozou (1987*a*) found that three-dimensional waves on the unbounded Rankine vortex are less unstable. Indeed, sufficiently short waves are stable, depending on the maximum Mach number M. Sozou (1987*b*) also found that for each azimuthal mode $m \geqslant 1$ and M, there is an infinite spectrum of unstable waves and that the wave considered by Broadbent & Moore (1979) is the first mode of the spectrum when the axial wave number tends to zero. For the case where the gas is rotating sufficiently fast such that a vacuum funnel exists at the centre of the vortex, Sozou & Wilkinson (1989) found both stable and unstable waves depending on m, M and the axial wavenumber.

This work has three parts. In the first part we study the linear stability of compressible vortices with smoother vorticity distributions than the Rankine vortex. Moore & Saffman (1973) showed how a smooth vorticity distribution arises from vortex sheet rollup; however, Dritschel (1988) showed that in the presence of strain, weak vorticity near the edge of the vortex core could be convected away and vorticity gradients sharpened. Since all analyses to date have assumed homentropic flow, we also study the effect of entropy gradient on the linear stability.

The second part of the project involves a numerical study of the linear initial-value problem. Finite-difference methods are frequently used in flow simulation programs such as ARC2D (Pulliam 1986*a*). These methods are less accurate than spectral methods, but are better able to accommodate arbitrary geometries. One of the main concerns of the present work is to investigate to what degree commonly employed finite-difference numerical techniques are able, and what enhancements are required, to accurately compute the sensitive instabilities in the vortex flows mentioned above. These numerical methods are then used to compute the linear and nonlinear behaviour of the flow. A further objective is to investigate the long-time behaviour of random perturbations which will reveal the least decaying behaviour of all perturbations at large time.

After obtaining some ideas on the effects of numerical parameters, the third part of this work involves the numerical simulation of the nonlinear development of perturbations.

The contents of the paper are as follows. In §2, the linear-stability analysis for arbitrary vorticity and entropy distributions are described. Singular points, boundary conditions and their numerical treatment are also discussed. Results of the linear-stability analysis are presented in §3. The behaviour of the far-field acoustic flux with Mach number is also computed. In §4, the numerical study of the linear initial-value problem is described. A linearized compressible Euler code is first developed using finite-difference methods and the effects of different numerical parameters are studied. Results of random initial perturbations are then provided. In §5, the nonlinear development of the perturbations is considered. The numerical method is described and then validated against linear theory. The long-time development of an elliptic mode perturbation and the behaviour of the far-field acoustic power are studied. A summary and discussion are given in §6.

After this paper was submitted, we learned of the low Mach number weakly nonlinear analysis of Crighton & Williams (1993) and Williams (1992) on the Broadbent & Moore (1979) instability. Their work showed that the instability grows until a time is reached when the instantaneous vortex radius in a particular direction vanishes, in agreement with our numerical results.

2. Linear-stability analysis

2.1. *Governing equations and solution methods*

The two-dimensional Euler equations in polar coordinates (r, θ) fixed in an inertial reference frame are

$$\frac{\partial v_r}{\partial t}+v_r\frac{\partial v_r}{\partial r}+\frac{v_\theta}{r}\frac{\partial v_r}{\partial \theta}-\frac{v_\theta^2}{r}=-\frac{1}{\rho}\frac{\partial p}{\partial r}, \quad \frac{\partial v_\theta}{\partial t}+v_r\frac{\partial v_\theta}{\partial r}+\frac{v_\theta}{r}\frac{\partial v_\theta}{\partial \theta}-\frac{v_r v_\theta}{r}=-\frac{1}{\rho r}\frac{\partial p}{\partial \theta}, \qquad (2.1\,a, b)$$

$$\frac{\partial \rho}{\partial t}+\frac{1}{r}\frac{\partial}{\partial r}(\rho r v_r)+\frac{1}{r}\frac{\partial}{\partial \theta}(\rho v_\theta)=0, \quad \frac{\partial S}{\partial t}+v_r\frac{\partial S}{\partial r}+\frac{v_\theta}{r}\frac{\partial S}{\partial \theta}=0, \qquad (2.1\,c, d)$$

where ρ is the density, p is the pressure, S is the specific entropy and v_r and v_θ are velocity components. An ideal gas with constant specific heats c_v and c_p is assumed with the equation of state

$$S = c_v \ln p - c_p \ln \rho + S_0, \qquad (2.1\,e)$$

where S_0 is a constant.

The steady basic-state flow is assumed to depend only on r and to have zero radial velocity. It is represented by variables with an overbar and satisfies

$$\frac{1}{\bar\rho}\frac{\mathrm{d}\bar p}{\mathrm{d}r}=\frac{\bar V_\theta^2}{r}, \quad \bar S = c_v \ln \bar p - c_p \ln \bar\rho + S_0. \qquad (2.2\,a, b)$$

Given any two of $\bar V_\theta$, $\bar S$, $\bar\rho$ and $\bar p$, the other two can be determined.

Small perturbations of normal-mode form are added to the basic-state variables, e.g.

$$v_\theta(r, \theta, t) = \bar V_\theta(r) + \tilde v_\theta(r)\,\mathrm{e}^{\mathrm{i}(\omega t + m\theta)}, \qquad (2.3)$$

where the eigenfunctions (such as $\tilde v_\theta(r)$) are complex and their real parts constitute the physical variables.

All variables are normalized by scaling with the respective physical quantities at $r = a$ where $\bar V_\theta$ is maximum (except for the pressure which is scaled by $\bar\rho \bar V_\theta^2$ at $r = a$). The reference Mach number M is defined to be the local Mach number at $r = a$. For convenience, S_0 is chosen such that $\bar S(a) = c_v$. The normalized radial coordinate x, the normalized eigenfrequency f, the normalized basic-state variables denoted by a circumflex, and the normalized eigenfunctions R, U, V, P for $\tilde\rho(r), \tilde v_r(r), \tilde v_\theta(r), \tilde p(r)$, respectively, are defined by

$$\left.\begin{array}{l} r = ax, \quad \omega = \dfrac{\bar V_\theta(a)}{a} f, \quad \bar\omega(r) = \dfrac{\bar V_\theta(a)}{a}\hat\omega(x), \quad \bar V_\theta(r) = \bar V_\theta(a)\,\hat V(x), \quad \bar S(r) = \bar S(a)\,\hat S(x), \\ \bar c(r) = \bar c(a)\,\hat c(x), \quad \bar\rho(r) = \bar\rho(a)\,\hat\rho(x), \quad \bar p(r) = \bar\rho(a)\,\bar V_\theta^2(a)\,\hat p(x), \\ \tilde\rho(r) = \bar\rho(a)\,R(x), \quad \tilde v_r(r) = \bar V_\theta(a)\,U(x), \quad \tilde v_\theta(r) = \bar V_\theta(a)\,V(x), \quad \tilde p(r) = \bar\rho(a)\,\bar V_\theta^2(a)\,P(x). \end{array}\right\} \qquad (2.4)$$

The linearized Euler equations then become

$$\frac{\mathrm{d}P}{\mathrm{d}x} = A(x)\,P + B(x)\,U, \quad \frac{\mathrm{d}U}{\mathrm{d}x} = C(x)\,P + D(x)\,U, \qquad (2.5\,a, b)$$

where
$$\left.\begin{aligned} A(x) &= \frac{\hat{V}^2M^2}{x\hat{c}^2}-\frac{2m\hat{V}}{x^2\hat{\sigma}}, \quad B(x) = \mathrm{i}\hat{\rho}\left(-\hat{\sigma}+\frac{2\hat{V}\hat{\omega}}{x\hat{\sigma}}-\frac{\hat{V}^2}{\gamma\hat{\sigma}x}\frac{\mathrm{d}\hat{S}}{\mathrm{d}x}\right), \\ C(x) &= \frac{\mathrm{i}}{\hat{\rho}}\left(\frac{m^2}{x^2\hat{\sigma}}-\frac{M^2\hat{\sigma}}{\hat{c}^2}\right), \quad D(x) = \frac{m\hat{\omega}}{\hat{\sigma}x}-\frac{\hat{V}^2M^2}{x\hat{c}^2}-\frac{1}{x}, \end{aligned}\right\} \tag{2.5c}$$

and
$$R = \frac{M^2}{\hat{c}^2}\left[P+\frac{\hat{p}}{\mathrm{i}\hat{\sigma}}\frac{\mathrm{d}\hat{S}}{\mathrm{d}x}U\right], \quad V = \frac{1}{\hat{\sigma}}\left[\frac{-mP}{\hat{\rho}x}+\mathrm{i}\hat{\omega}U\right], \tag{2.6a, b}$$

with
$$\hat{\sigma} = f+m\left(\frac{\hat{V}}{x}\right), \quad \hat{\omega} = \frac{\mathrm{d}\hat{V}}{\mathrm{d}x}+\frac{\hat{V}}{x}, \tag{2.7a, b}$$

where $\hat{c}$ and $\hat{V}$ are the normalized sound speed and tangential velocity respectively.

Given the basic-state solution and the boundary conditions at zero and infinity, the system (2.5*a*, *b*) defines an eigenvalue problem for the complex frequency $f \equiv f_r + \mathrm{i}f_i$. The angular phase frequency (henceforth referred to as the frequency) is given by f_r and $-f_i$ gives the growth rate.

It is physically necessary to assume that the pressure and radial-velocity perturbations, P and U, are finite and continuous everywhere. Since the right-hand sides of (2.5*a*, *b*) contain the vorticity $\hat{\omega}$ explicitly, a discontinuity in $\hat{\omega}$ implies a discontinuity in both $\mathrm{d}P/\mathrm{d}x$ and $\mathrm{d}U/\mathrm{d}x$. This is true, for example, for the Rankine vorticity profile. From (2.6*b*), the eigenfunction for tangential velocity V is discontinuous where $\hat{\omega}$ is discontinuous (unless $U = 0$ at the $\hat{\omega}$ discontinuity).

For arbitrary basic states, the solution to (2.5*a*, *b*) can only be obtained numerically. The singular points of the ordinary differential equation (ODE) set have to be analysed with care. The boundary condition at zero is that the perturbations must remain bounded, while the solution at infinity is taken to correspond to outward-going waves (incoming waves which correspond to a forced flow are not considered in this analysis). It can be shown that the ODE system for incompressible flow can be obtained by setting $M = 0$ and $\hat{c}^2 = \hat{\rho} = 1$. The condition at infinity is replaced by the condition of vanishingly small perturbations.

The complex eigenfrequency f is obtained iteratively by applying a numerical integration scheme to the ODE system (2.5*a*, *b*) and matching at some $x = x_{\mathrm{match}}$. The value of f is iterated by a Newton method until P/U is matched at x_{match}. Then, the values of P and U can be matched by choice of free eigenconstants. Convergence is typically achieved in about 5 to 8 steps for the cases considered.

2.2. *Basic-state variables*

Relations satisfied by the basic-state variables are derived below. Continuity of the flow variables is assumed everywhere except at a finite number of locations away from the origin. Viscous effects on the basic state in the linear-stability analysis can be disregarded provided the viscous timescale is much greater than the instability timescale; or $Re \gg -1/f_i$ where $Re \equiv a\bar{V}_\theta(a)/\nu$ and $-f_i$ is the normalized growth rate. For the cases considered in §3, $Re \gg 10^2$ is required. Khorrami (1991) and Duck & Khorrami (1991) have shown that for an incompressible trailing vortex with axial flow, viscosity can destabilize modes which are inviscidly neutral. Their growth occurs on the viscous timescale. It is possible that similar modes occur in the present situation but a viscous analysis is beyond the scope of the present work.

The assumption of uniform entropy has been frequently used in previous work to simplify the analysis. However, compressible vortices generated from boundary-layer separation are typically non-homentropic due to viscous heating. For steady axisymmetric vortices, Crocco's theorem reduces to

$$\bar{V}_\theta \bar{\omega} = \frac{\mathrm{d}\bar{H}}{\mathrm{d}r} - \bar{T}\frac{\mathrm{d}\bar{S}}{\mathrm{d}r}, \tag{2.8}$$

where $\bar{T}$ and $\bar{H} = c_v \bar{T} + \bar{p}/\bar{\rho} + \frac{1}{2}\bar{V}_\theta^2$ are the temperature and the total enthalpy of the basic state, respectively. Hence homentropic flow implies that the total enthalpy must vary in the vortical region. On the other hand, if the total enthalpy is constant in this region, then the flow must be non-homentropic. In general, both the entropy and total enthalpy are non-constant.

Typically, the basic-state vorticity $\hat{\omega}(x)$ and entropy $\hat{S}(x)$ distributions are given and the other flow variables are to be found in terms of these. Given $\hat{\omega}$, integration of (2.7*b*) gives $\hat{V}$:

$$\hat{V}(x) = \frac{1}{x}\int_0^x \alpha\hat{\omega}(\alpha)\,\mathrm{d}\alpha. \tag{2.9}$$

The normalized sound speed $\hat{c}$ is given by

$$\hat{c}^2 = \gamma M^2 \hat{p}/\hat{\rho}. \tag{2.10}$$

From (2.2*b*), the normalized entropy can be written as

$$\hat{S} = \ln(\gamma M^2 \hat{p}/\hat{\rho}^\gamma) + 1. \tag{2.11}$$

By defining

$$\left.\begin{aligned} \hat{S}_\gamma(x) &\equiv (\hat{S}(x) - 1)/\gamma, \\ \hat{I}(x) &\equiv \int_0^x \frac{\hat{V}^2(\alpha)}{\alpha}\mathrm{e}^{-\hat{S}_\gamma(\alpha)}\,\mathrm{d}\alpha, \\ \hat{I}_c(x) &\equiv 1 + (\gamma - 1)M^2[\hat{I}(x) - \hat{I}(1)], \end{aligned}\right\} \tag{2.12}$$

the normalized pressure, density and sound speed can be evaluated as follows:

$$\hat{p} = (1/(\gamma M^2))\hat{I}_c^{\gamma/(\gamma-1)}, \quad \hat{\rho} = \hat{I}_c^{1/(\gamma-1)}\mathrm{e}^{-\hat{S}_\gamma}, \quad \hat{c}^2 = \hat{I}_c \mathrm{e}^{\hat{S}_\gamma}. \tag{2.13}$$

By imposing $\hat{p}(0) > 0$, the following Mach number restriction is obtained:

$$M < \left(\frac{1}{(\gamma - 1)\hat{I}(1)}\right)^{\frac{1}{2}}. \tag{2.14}$$

Increasing the Mach number has the effect of lowering the minimum pressure until it reaches zero, which corresponds to a vortex evacuated at the centre. Further increasing the Mach number beyond the bound in (2.14) will result in a finite evacuated region. This regime is excluded from the present analysis.

2.3. *Singular points and boundary conditions*

2.3.1. *Singular points of the ODE system*

The ODE set (2.5*a*, *b*) can be cast into second-order form as follows:

$$\frac{\mathrm{d}^2 P}{\mathrm{d}x^2} + b_P(x)\frac{\mathrm{d}P}{\mathrm{d}x} + c_P(x)P = 0, \quad \frac{\mathrm{d}^2 U}{\mathrm{d}x^2} + b_U(x)\frac{\mathrm{d}U}{\mathrm{d}x} + c_U(x)U = 0, \tag{2.15}$$

where

$$\left.\begin{aligned} b_P(x) &= -\left(A + D + \frac{B'}{B}\right), \quad c_P(x) = A\frac{B'}{B} - A' + AD - BC, \\ b_U(x) &= -\left(A + D + \frac{C'}{C}\right), \quad c_U(x) = D\frac{C'}{C} - D' + AD - BC, \end{aligned}\right\} \tag{2.16}$$

x	Mach no.	$A(x)$	$B(x)$	$C(x)$	$D(x)$	b_P, b_U	c_P, c_U
0	$M \geqslant 0$	$O(x^{-1})$	$O(1)$	$O(x^{-2})$	$O(x^{-1})$	$O(x^{-1})$	$O(x^{-2})$
∞	$M > 0$	$O(x^{-3})$	$O(1)$	$O(1)$	$O(x^{-1})$	$O(x^{-1})$	$O(1)$
∞	$M = 0$	$O(x^{-3})$	$O(1)$	$O(x^{-2})$	$O(x^{-1})$	$O(x^{-1})$	$O(x^{-2})$

TABLE 1. Leading orders of expansions of A, B, C, D, b_P, b_U, c_P, c_U for $f \neq 0$ and non-homentropic flow

and the prime denotes differentiation with respect to x. In order to determine the nature of the singular points for this system, the series expansions of the basic-state variables $\hat{\omega}$, $\hat{V}$, $\hat{c}^2$, $\hat{\rho}$ and $\mathrm{d}\hat{S}/\mathrm{d}x$ in powers and inverse powers of x at $x = 0$ and $x = \infty$ respectively are required. The expansions are then substituted into A, B, C, D.

All flow variables are assumed to be finite and continuously differentiable at the origin. For many vortex flows observed in practice, the region near the centre approximates that of solid-body rotation. Hence, the leading constant term in the Taylor expansion for $\hat{\omega}$ is non-zero. For homentropic flow, the equations in §2.2 imply that the expansions for $\hat{c}^2$ and $\hat{\rho}$ go in even powers of x. For non-homentropic flow, the entropy gradient is assumed to consist of odd powers of x only. This form of the expansion has been guided by the analytically fitted empirical profiles of Mandella (1987).

For large x, the expansion of $\hat{\omega}$ in inverse powers of x is zero while the expansion of $\hat{V}$ contains only a single non-zero term in x^{-1}. For homentropic flow, the expansions for $\hat{\rho}$ and $\hat{c}^2$ as $x \rightarrow \infty$ consist of inverse even powers of x. Again guided by Mandella's empirical profiles, the entropy gradient for non-homentropic flow as $x \rightarrow \infty$ is assumed to have an expansion consisting of inverse odd powers of x starting at the x^{-3} term.

The resulting leading orders of the expansions for A, B, C, D for non-zero f and non-homentropic flow at $x = 0$ and as $x \rightarrow \infty$ are given in table 1.

For both compressible and incompressible flow, $x = 0$ is a regular singular point. However, at $x = \infty$, the BC term in (2.16) for the compressible case is $O(1)$, which implies $x = \infty$ is an irregular singular point. For the incompressible case, the BC term is $O(x^{-2})$ and so $x = \infty$ is a regular singular point. For $f = 0$, it can be shown that both $x = 0$ and $x = \infty$ are regular singular points for both incompressible and compressible flows.

2.3.2. *Boundary conditions*

Since $x = 0$ is a regular singular point, a series solution of the following form exists:

$$P = x^m(P_0 + P_2 x^2 + \ldots), \quad U = x^{m-1}(U_0 + U_2 x^2 + \ldots), \tag{2.17}$$

where the constants $U_0, P_2, U_2, \ldots$ can be expressed in terms of P_0 and the coefficients in the series expansions of the basic state. In the numerical work that follows, it is found that sufficient accuracy is attained with just the first term in the series.

An irregular singular point is located at infinity for compressible flow. The order of the expansions in inverse powers of x for b_P, b_U, c_P and c_U given in table 1 implies that an asymptotic solution of the following form exists (see Ince 1926, §7.3):

$$P \sim \left[p_0^* x^{-\frac{1}{2}} \exp\left(-\frac{\mathrm{i}fMx}{\hat{c}(\infty)}\right)\right]\left(1 + \frac{p_1^*}{x} + \ldots\right), \tag{2.18a}$$

$$U \sim \left[u_0^* x^{-\frac{1}{2}} \exp\left(-\frac{\mathrm{i}fMx}{\hat{c}(\infty)}\right)\right]\left(1 + \frac{u_1^*}{x} + \ldots\right), \tag{2.18b}$$

where $p_0^*, u_0^*, p_1^*, u_1^*, \ldots$ are constants and the u constants can be expressed in terms of the p constants, e.g.

$$u_0^* = \frac{M}{\hat{\rho}(\infty)\,\hat{c}(\infty)} p_0^*. \tag{2.18c}$$

The solution with a positive sign in the argument of the exponential is rejected because it does not represent outward-going waves. Broadbent & Moore (1979) arrived at the same form as (2.18) by a different approach which considers a uniform medium at rest. For incompressible flow, the point at infinity is a regular singular point, and admits a Frobenius series solution.

2.3.3. *Singularities due to zeros of* $\hat{\sigma}$

The complex zeros of $\hat{\sigma} = f + m(\hat{V}/x)$ are singular points of (2.5*a*, *b*). For cases close to neutral stability, the imaginary part of f is a small number, and the $\hat{\sigma}$-roots lie very close to the real axis. There may still be problems with integration along the real axis near these roots since the magnitude of the right-hand side will become very large relative to the values of P and U and accuracy may be lost.

Broadbent & Moore (1979) used the Riccati formulation which eliminates this problem for cases where the zero of $\hat{\sigma}$ falls in the region of zero vorticity, which is the case for the Rankine vortex. For cases where the zero of $\hat{\sigma}$ lies in the vortical region and for cases where the vorticity extends to infinity, the Riccati formulation does not remove the singularity.

Another method that can be used is to deform the contour of integration around the singularity in the complex plane. This requires analytic continuation of the basic-state variables into the complex plane, which is not valid in the neighbourhoods where any of these variables have discontinuities in the first derivative. In cases where the discontinuities of the basic state lie away from the deformed contour of integration, this technique has given us good results. However, for the truncated Gaussian profiles considered in §3.3, the singularity and the deformed contour of integration get closer and closer to the discontinuity of the basic state and this method fails.

The major obstacle in the singular-point analysis of the zero of $\hat{\sigma}$ is that its location is unknown in advance. Also, unlike the points $x = 0$ and $x = \infty$, the basic-state variables for different cases do not necessarily have the same form at the zero of $\hat{\sigma}$. Generalization can only be achieved if the zero of $\hat{\sigma}$ falls within the region of zero vorticity where $\hat{V}$ decays like x^{-1}. For a similar reason, the entropy is assumed to be constant in the region of zero vorticity.

Let x_s be the real zero of $\hat{\sigma}$ located in the irrotational region and let $\zeta = x - x_s$. Since the basic-state sound speed and density are analytic everywhere, the above then implies that b_U and c_U are regular, i.e. the ODE for U does not have a singular point at $x = x_s$ for either compressible or incompressible cases. However, b_P is $O(\zeta^{-1})$ and c_P is $O(\zeta^{-2})$, so $x = x_s$ is a regular singular point of the ODE for P. The resulting exponent of ζ in the leading term of the Frobenius series for P is positive. So there is actually no 'singular behaviour' at x_s if it lies within the region of zero vorticity and constant entropy. This is indeed true for most of the cases considered in the next section. In the numerical integration, A and C that contain $1/\hat{\sigma}$ are multiplied by P. So a very large number is multiplied by a very small number. With the high-precision floating-point representation on the CRAY-2, the round-off error that may arise from this is maintained within acceptable limits.

3. Results of linear-stability analysis for various cases

3.1. *Rankine vorticity profile*

Broadbent & Moore (1979) considered the compressible homentropic Rankine vortex with vorticity profile $\hat{\omega}(x)$ given by

$$\hat{\omega}(x)=\begin{cases}2, & 0\leqslant x\leqslant 1,\\ 0, & x>1.\end{cases}\tag{3.1}$$

The Mach number restriction given in (2.14) reduces to $M<(2/(\gamma-1))^{\frac{1}{2}}$.

The eigenfrequencies obtained by the shooting method described in §2 compare extremely well with those obtained by the Riccati formulation used by Broadbent & Moore (1979). The angular phase velocity of the mth mode is $(-f_r/m)$. Since $-m<f_r<0$, the wave travels in the same direction as that of the basic flow and has an angular speed of less than unity. Thus it rotates slower than the core, which rotates at an angular speed of one.

The discontinuity of the tangential velocity eigenfunction V, and the discontinuity in the derivative of the other eigenfunctions at $x=1$ are due to the discontinuity of vorticity at this location. A more satisfactory explanation for this jump is that the radial perturbation velocity, which is of order ϵ, causes the boundary of the vortical region to oscillate by a distance of the same order. The shapes of the linear eigenfunctions cannot depend on ϵ, and hence the eigenfunctions cannot give information about a region of width $O(\epsilon)$. Therefore, the behaviour of the eigenfunctions in such a region can only be represented by a finite jump in the value or slope at $x=1$. In order to obtain information about this region, the use of Lagrangian analysis is required, e.g. by consideration of the perturbed shape of the boundary of the vortical region as is done by Lamb (1932, §158) for the incompressible case.

It was suggested by Broadbent & Moore (1979) that the instability of the compressible vortex is triggered by the ability of the system to radiate acoustic waves, which allows the perturbations to extract energy from the mean flow. The sources and sinks of perturbation energy can be examined by considering the evolution equation of a positive definite energy-like quantity (Broadbent & Moore 1979). For homentropic flow, the growth of the perturbation energy is governed by the phase difference between the complex eigenfunctions P and U.

In figure 1(*a*), the real part of $\hat{\sigma}$ and the phase difference between the complex eigenfunctions P and U are plotted against x for the incompressible case. The phase difference between P and U is piecewise constant and is exactly $\frac{1}{2}\pi$ to the left and $\frac{3}{2}\pi$ to the right of a transition point that coincides with the zero of $\hat{\sigma}$. This can be seen from the exact solution for the incompressible eigenfunctions:

$$U=\begin{cases}mx^{m-1}, & x\leqslant 1,\\ mx^{-m-1}, & x>1,\end{cases}\tag{3.2a}$$

$$P=\begin{cases}\mathrm{i}x^{m}, & x\leqslant 1,\\ \mathrm{i}(1-m+mx^{-2})x^{-m}, & x>1.\end{cases}\tag{3.2b}$$

U is real and positive and hence $\arg(U)=0$, while P is imaginary with only one simple zero and it coincides with the zero of $\hat{\sigma}$. So P changes sign at the zero of $\hat{\sigma}$ which implies $\arg(P)-\arg(U)$ goes from $\frac{1}{2}\pi$ to $\frac{3}{2}\pi$.

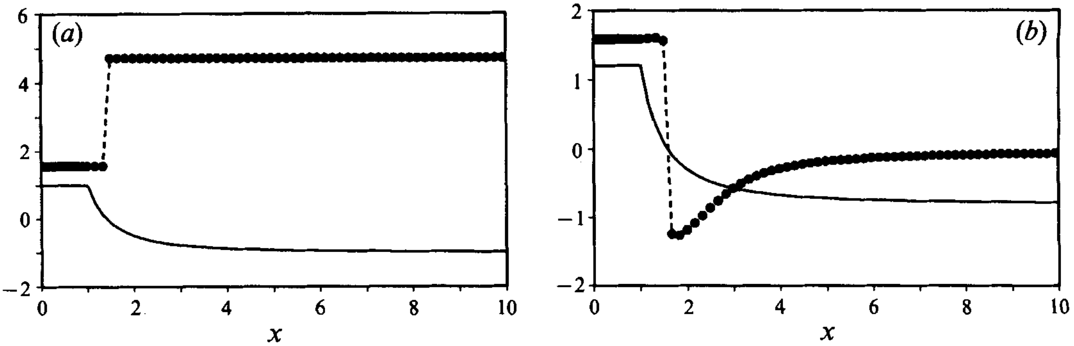

FIGURE 1. Plot of Re$(\hat\sigma)$ and phase difference between P and U for the Rankine vortex with $m=2$: ——, Re$(\hat\sigma)$; ---●---, arg$(P)-$arg(U). (*a*) Incompressible, (*b*) compressible with $M=1.5$.

Figure 1(*b*) shows the corresponding plot for a compressible case. The phase difference between P and U is no longer a constant. For the present case, the zero of $\hat\sigma$ is slightly off the real axis in the complex plane. The zero of P is still close to the zero of $\hat\sigma$ and hence it is expected to have a small imaginary part. Therefore the transition point of the phase difference between P and U still occurs very close to where the real part of $\hat\sigma$ goes to zero, as shown in figure 1(*b*).

It is suspected that $f=0$ is a solution for the $m=1$ mode. By setting f to zero and then marching P and U from zero and the far field to the matching point, it was found that the values of P/U on each side of the matching point agree to $\approx 10^{-7}$. It was then concluded that $f=0$ is a solution for the $m=1$ mode for compressible homentropic flow.

3.2. *Results for vorticity profiles with transition regions*

A study is performed on continuous vorticity profiles to determine whether the instability is peculiar to the Rankine vortex. Two vorticity profiles are considered in which a transition region of width δ exists between the constant value near the core centre and zero value outside.

The first vorticity profile has a linear-transition region. The normalized vorticity is given by

$$\hat\omega(x)=\begin{cases}2\Omega a/\bar V_\theta(a), & 0\leqslant x\leqslant \hat b-\hat\delta,\\ (2\Omega a\hat b/(\bar V_\theta(a)\,\hat\delta))(1-x/\hat b), & \hat b-\hat\delta< x\leqslant \hat b,\\ 0, & x>\hat b,\end{cases}\tag{3.3}$$

where Ω is the angular velocity of the inner solid-body rotation region, b is the dimensional size of the vortical region, $\hat\delta=\delta/a$ is the normalized width of the linear-transition region and $\hat b\equiv b/a$. Also we define $\delta'\equiv\delta/b$.

The second vorticity profile has a cosine transition region. Unlike the first case, this profile has no discontinuity in slope. The normalized vorticity is given by

$$\hat\omega(x)=\begin{cases}2\Omega a/\bar V_\theta(a), & 0\leqslant x\leqslant \hat b-\hat\delta,\\ (\Omega a/\bar V_\theta(a))[1+\cos(x_\delta)], & \hat b-\hat\delta< x\leqslant \hat b,\\ 0, & x>\hat b,\end{cases}\tag{3.4}$$

where $x_\delta\equiv(\pi/\hat\delta)(x-\hat b+\hat\delta)$.

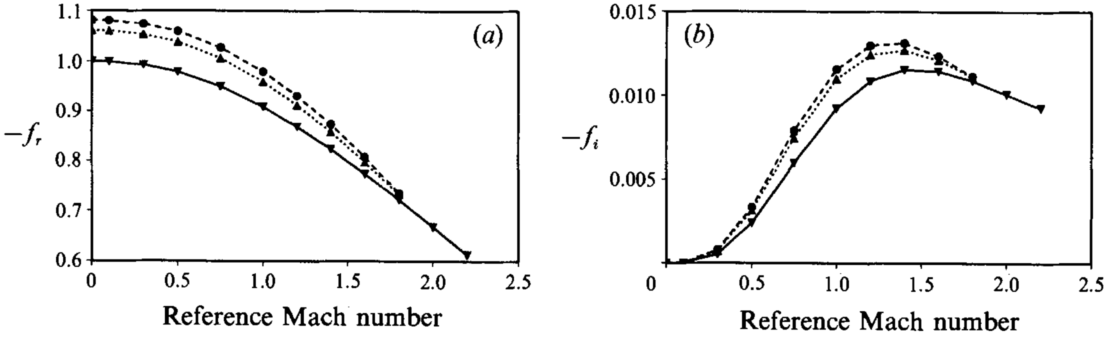

FIGURE 2. Comparison of (*a*) frequencies f_r and (*b*) growth rates $-f_i$ for the Rankine vortex and for basic-state vorticities with transition regions ($\delta' = 0.5$, $m = 2$): —▼—, Rankine; ---●---, linear transition; ···▲···, cosine transition.

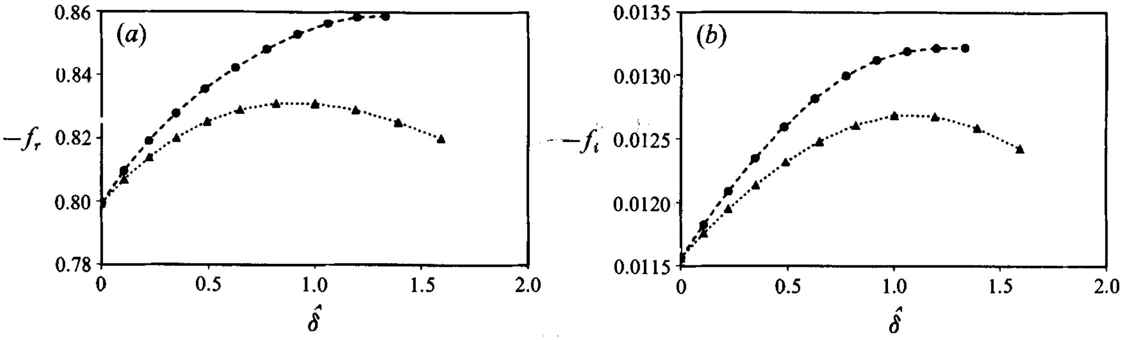

FIGURE 3. Variation of (*a*) frequencies f_r and (*b*) growth rates $-f_i$ with transition width $\hat{\delta}$ for basic-state vorticities with transition regions ($m = 2$, $M = 1.5$): ---●---, linear transition; ···▲···, cosine transition.

For a particular δ', the variations of f_r and f_i with Mach number are similar to those for the Rankine vortex (see figure 2*a*, *b*). The effect of different $\hat{\delta}$ is shown in figure 3(*a*, *b*) where $\hat{\delta} = 0$ corresponds to the Rankine vortex. Note that with the normalization used, the maximum $\hat{V}$ and its x-location remain fixed as $\hat{\delta}$ is varied.

For the linear transition profile, the magnitudes of both f_r and f_i increase with $\hat{\delta}$. It appears from the plots that the rate of increase tends to zero as $\hat{\delta}$ tends to its upper bound of $\frac{4}{3}$ (corresponding to a δ' of 1.0) where the region of solid-body rotation has shrunk to zero. So the instability of vortices of this type increases with increasing $\hat{\delta}$ if the vortices have the same maximum velocity.

For the cosine transition profile, both f_r and f_i peak at about $\hat{\delta} = 1.0$ (corresponding to $\delta' = 0.7$). This behaviour is quite different from that of the linear-transition case. At a given $\hat{\delta}$, the linear transition case is more unstable than the cosine transition case. However, it was found that when a different normalization scheme is used (keeping total circulation constant), the cosine transition case becomes more unstable than the linear transition case.

The P eigenfunction for the cosine transition case with $m = 2$, $M = 1.5$ and $\delta' = 1.0$ is plotted in figure 4(*a*, *b*). The overall behaviour is similar to that of the Rankine case, except that here all the eigenfunctions are continuous and have continuous derivatives everywhere. For this reason, this case is used as one of the initial

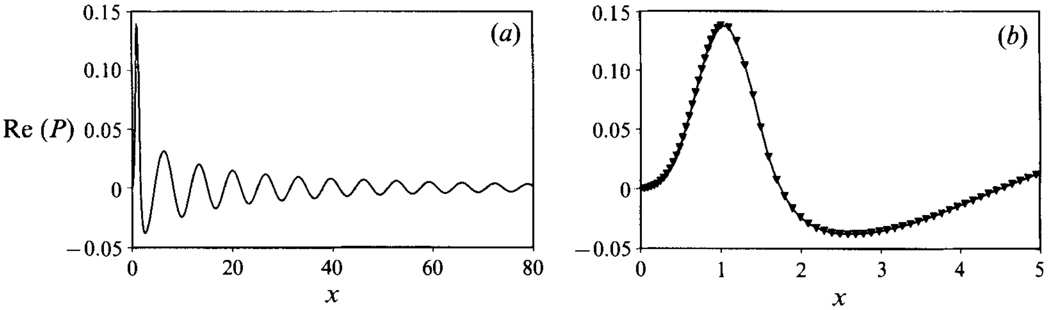

FIGURE 4. Real part of P eigenfunction for basic state with cosine-transition vorticity ($\delta' = 1.0$, $m = 2$, $M = 1.5$). (*a*) Far-field behaviour, (*b*) inner-region behaviour.

conditions for the study of the linear initial-value problem in §4 and the nonlinear problem in §5.

3.3. *Gaussian and truncated-Gaussian vorticity profiles*

The goal of this section is to study a case where the vorticity has continuous derivatives to infinite order, extends to infinity and decays exponentially with distance from the origin. The Gaussian vorticity profile is chosen for this purpose. Also, it is a solution at an instant of a diffusing circular potential vortex under the action of viscosity (Lamb 1932, §334*a*).

Convergence was not obtained despite numerous trials with different starting guesses, iteration methods and integration schemes. In order to investigate the source of the difficulty, a family of Gaussian vorticity profiles truncated at $x = \xi$ is considered such that the full Gaussian profile is recovered when ξ goes to infinity. The normalized vorticity is given by

$$\hat{\omega}(x) = \begin{cases} 2\kappa \mathrm{e}^{-\kappa x^2}/(1-\mathrm{e}^{-\kappa}), & 0 \leqslant x \leqslant \xi, \\ 0, & x > \xi, \end{cases} \tag{3.5}$$

where the parameter κ is chosen such that the maximum $\hat{V}$ occurs at $x = 1$. In order to have the same position of maximum $\hat{V}$ for different members of the sequence, the restriction $\xi \geqslant 1$ is imposed. With this scaling, ξ has to be of the order of only 4 or 5 before the profile becomes practically Gaussian.

The eigenfrequencies for different values of ξ are obtained for three different reference Mach numbers starting from $\xi = 1$ (see figure 5*a*, *b*). The incompressible limit ($M = 0$) is found to be neutrally stable. Both f_r and f_i decrease with increase of ξ and the growth rates for the compressible cases quite rapidly approach zero as ξ becomes large. The trends suggest that the Gaussian vortex is neutrally stable for all reference Mach numbers. Convergence becomes increasingly difficult as ξ is increased until $\xi \approx 2.4$ where no convergence is obtained. Note that the position of the zero of $\hat{\sigma}$ is in the region of zero vorticity for small values of ξ and asymptotes towards the boundary of the region of non-zero vorticity as ξ increases (figure 6*a*, *b*). This makes deformation of the contour of integration more and more difficult. For all the vorticity profiles considered up to this point, the zero of $\hat{\sigma}$ lies at a finite distance away from the boundary of the region of non-zero vorticity and there were no problems in convergence. As discussed in §2.3, if the zero of $\hat{\sigma}$ approaches the region of non-zero vorticity, the singular-point behaviour may depart from being regular. When this happens, convergence difficulties are observed.

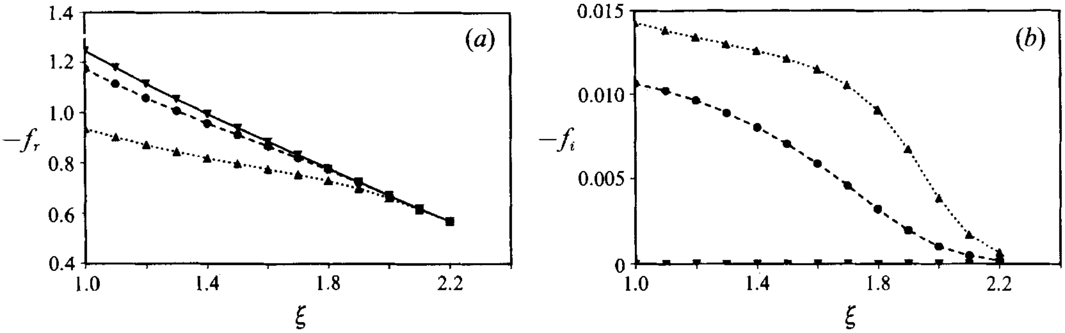

FIGURE 5. Variation of (*a*) frequencies f_r and (*b*) growth rates $-f_i$ with ξ for the truncated-Gaussian vorticity profile with $m = 2$ and different reference Mach numbers M: —·—▼—·—, $M = 0$; ---●---, $M = 0.8$; ···▲···, $M = 1.5$.

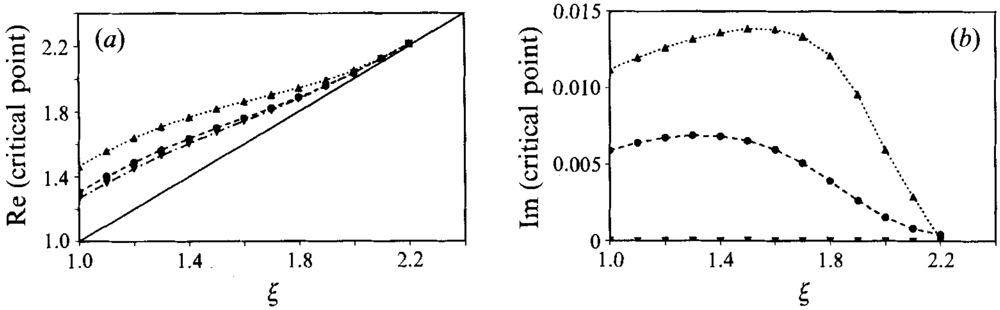

FIGURE 6. (*a*) Real part and (*b*) imaginary part of the zero of $\tilde{\sigma}$ against ξ for the truncated-Gaussian vorticity profile with $m = 2$ and different reference Mach numbers M: —·—▼—·—, $M = 0$; ---●---, $M = 0.8$; ···▲···, $M = 1.5$; ——, reference line.

3.4. *Effect of entropy gradient*

In this subsection, the effect of non-constant entropy for the Rankine vortex is investigated. The choice of an entropy profile for a model problem is guided by the experiments of Mandella (1987). Since the vortices he generated were unsteady, they cannot be used as basic states in the stability analysis. However, a model entropy profile can be constructed based on his results. Inside the constant-vorticity region, the entropy behaviour near the origin of Mandella's vortex is used. In the irrotational region, the entropy is set to a constant chosen to preserve continuity at the boundary of the two regions.

The expression for $\hat{S}$ represents a family of entropy profiles given by

$$\hat{S}(x) = \begin{cases} 1-\hat{S}_2(1-x^2), & 0 \leqslant x \leqslant 1, \\ 1, & x > 1, \end{cases} \tag{3.6}$$

where the parameter $\hat{S}_2$ is the average entropy gradient in the core. Both the entropy gradient and the vorticity which appear on the right-hand side of the ODE system (2.5*a*, *b*) are discontinuous at $x = 1$. The behaviour of Mandella's vortex near the origin corresponds to a value of $\hat{S}_2$ approximately equal to 1.0. An example of a case where the entropy decreases with distance from the vortex centre, corresponding to a negative $\hat{S}_2$, can be found in the rolled-up vortices in mixing layers (Sandham 1989).

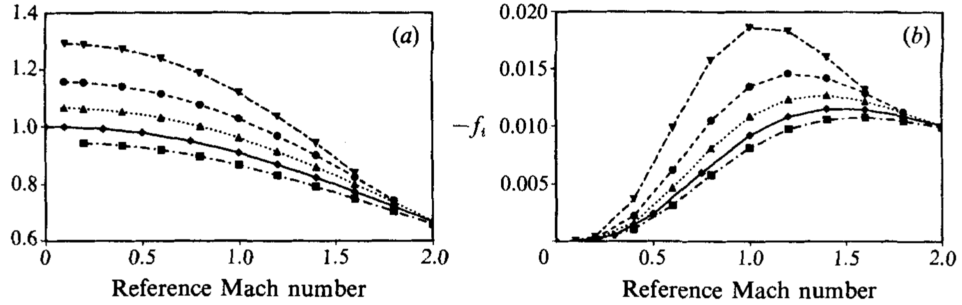

FIGURE 7. (*a*) Frequencies f_r and (*b*) growth rates $-f_i$ for different values of $\hat{S}_2$ for the non-constant-entropy model problem ($m = 2$): – –▼– –, $\hat{S}_2 = 1.5$; – – –●– – –, $\hat{S}_2 = 1.0$, ·······▲·······, $\hat{S}_2 = 0.5$; ——◆——, $\hat{S}_2 = 0$; —·—■—·—, $\hat{S}_2 = -0.5$.

Figure 7(*a, b*) shows the variations of f_r and f_i with reference Mach number M for several values of $\hat{S}_2$ for the $m = 2$ mode. The results indicate that a positive average entropy gradient tends to destabilize the vortex while a negative average entropy gradient has the opposite effect. The peak of $-f_i$ occurs at a lower M as $\hat{S}_2$ is increased. For a given reference Mach number M, the magnitudes of both f_r and f_i increase with $\hat{S}_2$.

The destabilizing effect of positive entropy gradient can be qualitatively understood by noting that the effective Brunt–Väisälä frequency (Howard 1973) can be written as

$$N^2 \equiv \frac{\bar{V}_\theta^2}{r}\left[\frac{1}{\bar{\rho}}\frac{\mathrm{d}\bar{\rho}}{\mathrm{d}r} - \frac{\bar{V}_\theta^2}{r\bar{c}^2}\right] = -\frac{\bar{V}_\theta^2}{\gamma r}\frac{\mathrm{d}\bar{S}}{\mathrm{d}r}, \tag{3.7}$$

i.e. positive entropy gradient corresponds to unstable stratification.

The variations of f_r and f_i with $\hat{S}_2$ for $m = 2$ and 3 at $M = 0.8$ were also computed. The trends for the two azimuthal mode numbers are similar. For a given $\hat{S}_2$, the $m = 3$ mode has a larger magnitude for f_r and a smaller magnitude for f_i relative to those for $m = 2$.

3.5. *Comparison of far-field acoustics with Lighthill's theory*

It is of interest to compare the acoustic flux predicted by linear-stability analysis with the seventh-power law of Lighthill (1952), valid for a two-dimensional sound source at low Mach numbers. The same power law was also obtained by Howe (1975) and Broadbent (1976) for the far-field acoustic energy flux of an elliptical vortex with small aspect ratio and constant core vorticity in low-Mach-number flow. It is worth noting that, according to Broadbent (1976), the elliptic mode is the most efficient, while the higher-order modes ($m > 2$) produce progressively higher-order poles which are less efficient.

The basic-state vorticity with a cosine transition is considered with $\delta' = 1.0$ and $m = 2$. Since the Mach number in Lighthill's theory is defined using the sound speed in the medium at rest, in this section only 'Mach number' will refer to M' defined by

$$M' = \bar{V}_\theta(a)/\bar{c}(\infty). \tag{3.8}$$

The far-field radial acoustic energy flux E_r is defined as

$$E_r = \int_0^{2\pi} r\overline{\tilde{p}\tilde{v}_r}\,\mathrm{d}\theta, \tag{3.9}$$

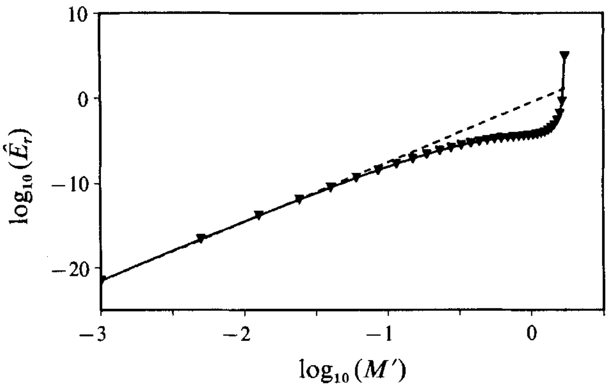

FIGURE 8. Variation of far-field radial acoustic energy flux with Mach number M' for the cosine vorticity case with $\delta' = 1.0$ and $m = 2$: —▼—, stability analysis; ----, low-Mach-number theory.

where an overbar denotes a time average. After defining a normalized far-field radial acoustic energy flux $\hat{E}_r$ referenced to far-field quantities,

$$\hat{E}_r = \frac{E_r}{a\bar{\rho}(\infty)\,\bar{c}^3(\infty)}, \tag{3.10}$$

one obtains

$$\hat{E}_r(x) = \frac{\bar{\rho}(a)}{\bar{\rho}(\infty)} M'^3 \pi x [\mathrm{Re}\,(P(x))\,\mathrm{Re}\,(U(x)) + \mathrm{Im}\,(P(x))\,\mathrm{Im}\,(U(x))]. \tag{3.11}$$

The variation of $\hat{E}_r$ at large x with Mach number M' is plotted on a log scale in figure 8 where the eigenfunctions are scaled with the constant P_0 set to 1 (see 2.17). It was ensured that x is large relative to the period of oscillation of P and U in the far field. As anticipated, the low-Mach-number result agrees with Lighthill's theory. The leading-order term for small M' in the expansion for $\bar{\rho}(a)/\bar{\rho}(\infty)$, the first factor in (3.11), is independent of M' (see §2.2). Hence the main contributions to the variation of $\hat{E}_r$ at low Mach numbers arise from the M'^3 factor and the PU product terms in (3.11) which must scale like M'^4. Substitution of the leading-order far-field behaviour of P and U given by (2.18*a*, *b*) into (3.11) indicates that the leading-order term for the quantity in square brackets in (3.11) is given by $\mathrm{Re}\,(p_0^*)\,\mathrm{Re}\,(u_0^*) + \mathrm{Im}\,(p_0^*)\,\mathrm{Im}\,(u_0^*)$. From (2.18*c*), u_0^* scales like $M' p_0^*$. The above then implies that p_0^* should scale like $M'^{\frac{3}{2}}$ and u_0^* should scale like $M'^{\frac{5}{2}}$, and likewise for P and U, for small M'. This result was also verified numerically.

At $M' \approx 0.3$, deviation from the low-Mach-number theory begins to appear. The dependence of $\hat{E}_r$ on M' is less powerful at higher Mach numbers. At $M' \approx 1.1$, a sharp increase in $\hat{E}_r$ is observed until the evacuation limit (2.14) is reached.

4. Linear initial-value problem

In this section, the linear evolution of arbitrary disturbances is considered. The purpose is three-fold: (i) to inquire whether cases that have neutral normal modes may support algebraic instabilities; (ii) to use random initial conditions to search for new types of normal-mode behaviour which may have been overlooked in the past; (iii) to investigate whether typical finite-difference methods used in research and production codes such as ARC2D, ARC3D (Pulliam 1986*a*) and F3D (Ying 1986) are sufficiently accurate to capture the weak instability of the present problem.

4.1. *Numerical methods for the linear initial-value problem*

The linearized unsteady two-dimensional Euler equations are solved with a finite-difference scheme. The normalized perturbation density, radial velocity, tangential velocity and pressure ($\tilde{R}$, $\tilde{U}$, $\tilde{V}$ and $\tilde{P}$ respectively) satisfy

$$\frac{\partial \boldsymbol{Q}}{\partial t}+\boldsymbol{A}_s\frac{\partial \boldsymbol{Q}}{\partial x}+\boldsymbol{B}_s\frac{\partial \boldsymbol{Q}}{\partial \theta}+\boldsymbol{F}=0, \tag{4.1}$$

where

$$\boldsymbol{Q}=\begin{bmatrix}\tilde{R}\\ \tilde{U}\\ \tilde{V}\\ \tilde{P}\end{bmatrix},\quad \boldsymbol{F}=\begin{bmatrix}((\hat{\rho}/x)+\mathrm{d}\hat{\rho}/\mathrm{d}x)\,\tilde{U}\\ -(1/\hat{\rho}^2)(\mathrm{d}\hat{p}/\mathrm{d}x)\,\tilde{R}-(2\hat{V}/x)\,\tilde{V}\\ \hat{\omega}\tilde{U}\\ (\hat{c}^2/M^2)((\hat{\rho}/x)+\mathrm{d}\hat{\rho}/\mathrm{d}x)\,\tilde{U}+\hat{p}(\mathrm{d}\hat{S}/\mathrm{d}x)\,\tilde{U}\end{bmatrix}, \tag{4.2a}$$

$$\boldsymbol{A}_s=\begin{bmatrix}0 & \hat{\rho} & 0 & 0\\ 0 & 0 & 0 & 1/\hat{\rho}\\ 0 & 0 & 0 & 0\\ 0 & \hat{\rho}\hat{c}^2/M^2 & 0 & 0\end{bmatrix},\quad \boldsymbol{B}_s=\begin{bmatrix}\hat{V}/x & 0 & \hat{\rho}/x & 0\\ 0 & \hat{V}/x & 0 & 0\\ 0 & 0 & \hat{V}/x & 1/(\hat{\rho}x)\\ 0 & 0 & \hat{\rho}\hat{c}^2/(M^2x) & \hat{V}/x\end{bmatrix}. \tag{4.2b}$$

The eigenvalues λ_A, λ_B of $\boldsymbol{A}_s$ and $\boldsymbol{B}_s$ are given by

$$\left.\begin{aligned}\lambda_A&=0,\quad 0,\quad \frac{\hat{c}}{M},\quad -\frac{\hat{c}}{M},\\ \lambda_B&=\frac{\hat{V}}{x},\quad \frac{\hat{V}}{x},\quad \frac{\hat{V}}{x}+\frac{\hat{c}}{Mx},\quad \frac{\hat{V}}{x}-\frac{\hat{c}}{Mx}.\end{aligned}\right\} \tag{4.3}$$

Various elements of the numerical scheme are described below. For further details, the reader is referred to Chan (1990).

Space derivatives are replaced by finite differences on a polar grid. In the azimuthal direction, a uniform grid spacing is used with fourth-order central differencing. In the radial direction, a fine uniform spacing Δx is used in the region $0 \leqslant x \leqslant 2$ and the grid is stretched outside this region. Let ζ and l be the stretched radial coordinate and grid point index, respectively. The partial derivatives are replaced by finite-difference operators δ_ζ as follows:

$$\partial/\partial x=\zeta_x\delta_\zeta. \tag{4.4}$$

In the evaluation of the metrics ζ_x, fourth- and second-order central differencing are used in the interior and at one point from the boundaries respectively. Two options for the radial differencing are implemented. The first uses fourth-order central differencing with a small amount of artificial dissipation. The second employs a flux-splitting formulation which requires the use of upwind or upwind-biased differencing schemes.

It is a well-known phenomenon that central differencing results in an odd–even uncoupling between grid points and gives the solution a sawtooth-like appearance. This is caused by slight inconsistencies or inaccuracies in the numerical boundary conditions and the aliasing errors from nonlinear terms. Some dissipative mechanism is required to damp out these numerical errors (Pulliam 1986*a*, *b*; Jameson, Schmidt & Turkel 1981).

For the present problem, a small amount of fourth-order dissipation (Pulliam 1986*b*) is applied in the radial direction. The dissipation term $\boldsymbol{D}_e$ added to the right-hand sides of the ODEs for time advance is

$$\boldsymbol{D}_e=-\Delta t\,\epsilon_\zeta(\nabla_\zeta\Delta_\zeta)^2\boldsymbol{Q}^n, \tag{4.5}$$

where ϵ_ζ is a non-negative parameter of $O(1)$ which controls the amount of dissipation, Δt is the time step, Q^n is the vector of dependent variables at time level n and the difference operators are defined by

$$\Delta_\zeta q_{j,l} = q_{j,l} - q_{j,l-1}, \quad \nabla_\zeta q_{j,l} = q_{j,l+1} - q_{j,l}. \tag{4.6}$$

The alternative to using central differencing with artificial dissipation is to use upwind-differencing in the radial direction, which can be shown to be equivalent to a central-differencing scheme (non-dissipative) plus an inherent amount of dissipation (Pulliam 1986*b*). The scheme that is employed here is similar to the split coefficient-matrix method developed by Chakravarthy (1979) and is described next.

Consider the Jacobian matrix $\boldsymbol{A}_s$ associated with the radial direction in (4.2). Let Λ be its diagonal eigenvalue matrix and $\boldsymbol{X}$ be its eigenvector matrix. A decomposition for Λ is,

$$\Lambda = \Lambda^+ + \Lambda^-, \tag{4.7}$$

where Λ^+ consists of all the positive eigenvalues and Λ^- consists of all the negative eigenvalues. Then, $\boldsymbol{A}^+, \boldsymbol{A}^-$ can be formed using

$$\boldsymbol{A}^{\pm} \equiv \boldsymbol{X}\Lambda^{\pm}\boldsymbol{X}^{-1} = \frac{1}{2}\begin{bmatrix} 0 & \hat{\rho} & 0 & \pm M/\hat{c} \\ 0 & \pm\hat{c}/M & 0 & 1/\hat{\rho} \\ 0 & 0 & 0 & 0 \\ 0 & \hat{\rho}\hat{c}^2/M^2 & 0 & \pm\hat{c}/M \end{bmatrix}, \tag{4.8}$$

where $\boldsymbol{A}_s = \boldsymbol{A}^+ + \boldsymbol{A}^-$ is satisfied. The radial derivative in (4.1) is then approximated by

$$\boldsymbol{A}_s \frac{\partial \boldsymbol{Q}}{\partial x} \approx \boldsymbol{A}^+ \zeta_x \delta^b_\zeta \boldsymbol{Q} + \boldsymbol{A}^- \zeta_x \delta^f_\zeta \boldsymbol{Q}, \tag{4.9}$$

where $\delta^b_\zeta, \delta^f_\zeta$ are backward and forward one-sided differencing operators, respectively. The following three one-sided schemes are considered: first-order upwind, second-order upwind and third-order upwind-biased given by respectively,

$$\delta^b_\zeta = q_l - q_{l-1}, \quad \delta^f_\zeta = q_{l+1} - q_l; \tag{4.10a}$$

$$\delta^b_\zeta = \tfrac{1}{2}(3q_l - 4q_{l-1} + q_{l-2}), \quad \delta^f_\zeta = \tfrac{1}{2}(-3q_l + 4q_{l+1} - q_{l+2}); \tag{4.10b}$$

$$\delta^b_\zeta = \tfrac{1}{6}(2q_{l+1} + 3q_l - 6q_{l-1} + q_{l-2}), \quad \delta^f_\zeta = \tfrac{1}{6}(-2q_{l-1} - 3q_l + 6q_{l+1} - q_{l+2}). \tag{4.10c}$$

The performance of these schemes is discussed in §4.3.

Time advancement is performed using the third-order Runge–Kutta scheme (RK3) of Wray (1986), which requires less storage than other typical RK3 schemes.

The boundary condition imposed at the origin is that all perturbation quantities vanish. This is required for smoothness at the origin for $m > 1$. In the far field, the condition of 'outward-going waves' has to be implemented. A non-reflective boundary treatment (Thompson 1987) is used to minimize 'incoming waves' from the far field. Although this scheme has been derived from a one-dimensional analysis, its use is justified in our two-dimensional problem since the dominant mode ($m = 2$) has variations tangential to the far-field boundary which are much smaller relative to the variations normal to the far-field boundary. The implementation of this scheme for the present problem is described in detail in Chan (1990).

For an inviscid flow, in the absence of viscosity and heat conduction, the entropy production is zero. Hence, a flow that is initially homentropic will remain so for subsequent times. For a homentropic basic state, the linear eigenfunctions are

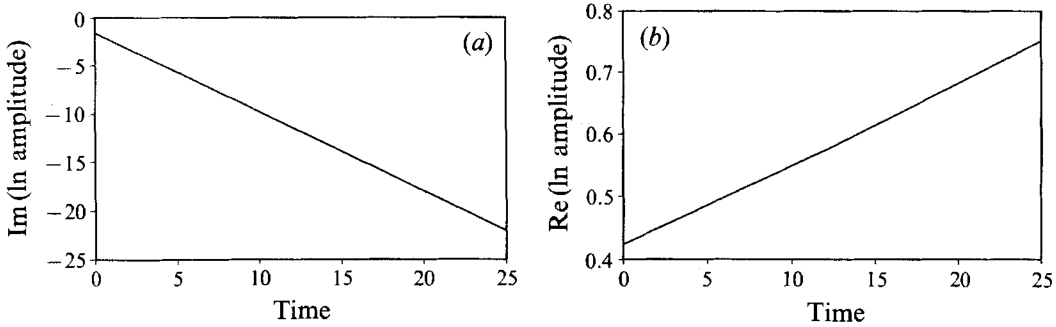

FIGURE 9. Natural log of amplitude of $m = 2$ mode for cosine-transition vorticity profile with $\delta' = 1$. (*a*) Slope = frequency, (*b*) slope = growth rate.

homentropic to linear order. For the computations described in §§4.2 and 4.3, in the presence of dissipation in the optimum range, the pointwise entropy error is typically about four orders of magnitude smaller than the maximum magnitude of the eigenfunctions initially and remains so during the computation.

Growth rates and frequencies are analysed by plotting the azimuthal Fourier coefficient (corresponding to a mode m) in log-linear coordinates at the radial location $x = 0.8$.

4.2. *Detailed study of a typical case*

The linear initial-value code is tested using eigenfunctions for the cosine-transition profile ($\delta' = 1, m = 2$ and $M = 1.5$) as initial conditions. In the azimuthal direction, the mesh is uniform with 128 points. In the radial direction, the mesh is made up of a fine uniform region in $0 \leqslant x \leqslant 2$ with 81 points and an exponentially stretched region in $2 \leqslant x \leqslant 20$ with 116 points. Fourth-order central space-differencing is used in both directions with $\epsilon_\xi = 0.5$. The time step used is 0.004 which is just inside the stability bound for RK3.

Figure 9(*a*, *b*) shows the log of the amplitude for the $m = 2$ mode. The plots are linear up to $t \approx 12$ and the slopes agree to within 0.2% with the eigenfrequencies computed by the shooting method described in §3. The amplitudes of other Fourier modes remain insignificant which implies that the finite-difference scheme has not introduced any spurious modes.

The agreement between the linear initial-value problem solution and the normal-mode solution was further confirmed by sampling the frequencies and growth rates at three different radial positions. Identical values were obtained, except for small differences at the far-field location where the resolution is poor.

4.3. *Effects of different numerical parameters*

We wish to briefly discuss the effects of different numerical parameters on the computed frequencies and growth rates. This establishes aspects of the method that must be treated with care in subsequent linear and nonlinear calculations. The case described in §4.2 is used as a base case for comparisons.

It is found that the numerical stability bound of the explicit time march scheme places a more stringent restriction on the time step than the requirement of resolving the smallest timescales of the instability.

The growth rate increases with the level of dissipation present in the scheme, but there is a range of values of the dissipation coefficient, $0.05 \leqslant \epsilon_\xi \leqslant 0.5$, that gives

ϵ_ξ	$-f_r$	$-f_i$
*	0.8201	0.01243
0	0.82009	0.012401
0.05	0.82009	0.012405
0.1	0.82009	0.012406
0.5	0.82008	0.012409
2.0	0.82006	0.012418

TABLE 2. Frequencies and growth rates for different dissipation coefficients ϵ_ξ at small time ($t < 2$) with fixed uniform interior radial grid spacing $\Delta x = 0.025$ (*, eigenvalue shooting method)

Δx	$-f_r$	$-f_i$
0.025	0.8201	0.01241
0.05	0.8200	0.01243
0.1	0.8197	0.01229
0.025*	0.8201	0.01244

TABLE 3. Frequencies and growth rates for different uniform interior radial grid spacing Δx at small time ($t < 2$) with fixed dissipation coefficient $\epsilon_\xi = 0.5$ (*, poor far-field resolution)

almost identical and accurate results (see table 2). The frequency is captured accurately for an even larger range of values of the dissipation coefficient. With the dissipation set to zero, the scheme is still able to give good results for small time before oscillations start to contaminate the solution.

There have been many computations of unsteady compressible flows in which a stretched mesh is used in the far field (e.g. Chen, Cantwell & Mansour 1989). The question then arises as to whether poor resolution of sound waves propagating in the far field would lead to errors in the inner field.

Four cases are studied. For the first three cases, three values of uniform $\Delta x (= 0.025, 0.05, 0.1)$ are used in the region $0 \leqslant x \leqslant 2$, while the mesh spacing is identical for the three cases in the stretched region (116 points used). In the fourth case, a fine uniform spacing of $\Delta x = 0.025$ is used in $0 \leqslant x \leqslant 2$ while the resolution in the stretched region is made to be very poor (56 points).

It is found that the growth rate is much more sensitive to the mesh resolution in the near field than in the far field, i.e. the inability to resolve the eigenfunction in the near field results in poor growth rates, while the inability to resolve the eigenfunctions in the far field still results in fairly accurate growth rates (see table 3). Again the frequency is not sensitive to changes in mesh resolution.

Results are obtained for cases using the three upwind-differencing schemes listed in (4.10*a–c*) with the split coefficient-matrix formulation. The growth rate obtained using the third-order scheme is nearly identical to that found with the fourth-order central differencing scheme with dissipation in the optimum range. The growth rate for the second-order scheme is slightly higher than that of the third-order scheme, while the growth rate of the first-order scheme is much higher than that of the second-order scheme. These results are consistent with the earlier observation that an increase in the level of dissipation results in an increase of the growth rate. It is found that the frequency is essentially independent of the choice of differencing schemes.

Runs with different far-field boundary locations keeping the inner resolution constant indicate that the results are not affected provided the far field is not located

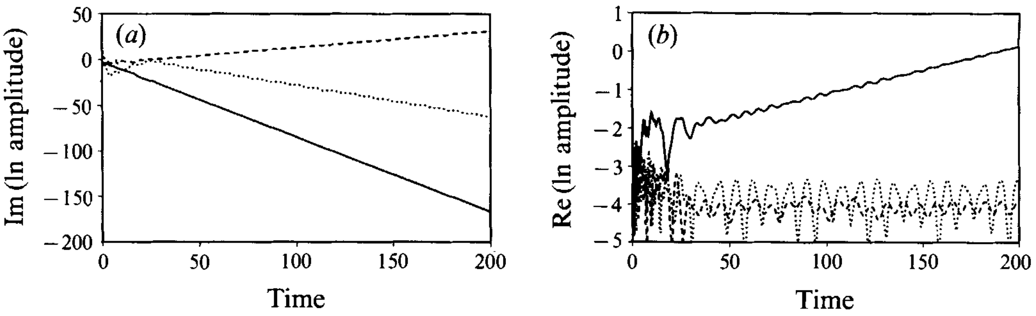

FIGURE 10. Natural log of amplitudes of $m = 2, 3, 4$ modes for cosine-transition vorticity profile with $\delta' = 1$ and random initial perturbations. (*a*) Slope = frequency, (*b*) slope = growth rate: ——, $m = 2$; – – –, $m = 3$; ········, $m = 4$.

too close ($x < 10$) to the vortex core. A test was performed to investigate the sensitivity of the far-field boundary treatment. Results identical to those found using the non-reflecting conditions are obtained for $t \leqslant 25$ when zeroth-order extrapolation is used for all four variables at the far-field boundary.

4.4. *Random initial perturbations*

Up to the previous section, the computations performed with the linear finite-difference code used eigenfunctions as initial conditions. With some knowledge of the sensitivity of the method to different numerical parameters, we can now perform studies using random initial conditions.

Since the Fourier modes in the periodic θ-direction form a complete set, a study of random behaviour in θ is not necessary. Hence, randomness is only introduced in the radial direction by the function $\tilde{q}_l$ whose magnitude is made to decay exponentially in the far field. The initial condition $\tilde{Q}_{j,l}$ is given by

$$\tilde{Q}_{j,l} = \tilde{q}_l(x) \sum_{m=2}^{N_m} \cos(m\theta_j), \tag{4.11}$$

where θ_j is the polar angle at the *j*th grid point in the azimuthal direction. Since the high-order azimuthal modes are expected to be close to neutrally stable, only small values of N_m are considered.

First, the basic state with cosine-transition vorticity ($\delta' = 1$) in §4.2 is considered with the $m = 2, 3, 4$ modes in θ excited ($N_m = 4$). The plots of log of amplitude in figure 10(*a*, *b*) show that the real and imaginary parts of the $m = 2$ mode eventually settle down to straight lines, indicating that the long-time behaviour contains an exponential term. On comparing the slopes of these lines at large time, it is found that they agree to at least three decimal places with the frequency and growth rate that we obtained from the shooting method.

For the $m = 3$ and 4 modes, the shooting code failed to converge when an initial guess close to the $m = 2$ eigenfrequency was used. Now, from figure 10(*a*, *b*), the growth rates for large time for both the $m = 3$ and 4 modes appear to be close to zero, and the long-time behaviour of the frequencies appears to be of the normal-mode type. This indicates the existence of nearly neutral normal-mode solutions for $m = 3$ and 4. Note that the frequency of the $m = 3$ mode is of the opposite sign to that of the $m = 2$ mode, i.e. the wave for $m = 3$ rotates in the opposite direction to that of the vortex. To verify this, the eigenvalue-shooting code was used with an initial guess that has a

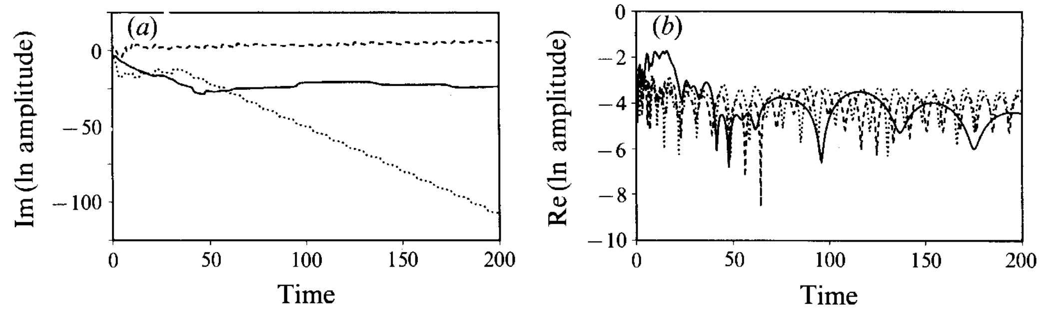

FIGURE 11. Natural log of amplitudes of $m = 2, 3, 4$ modes for Gaussian vorticity profile with random initial perturbations. (*a*) Slope = frequency, (*b*) slope = growth rate: ——, $m = 2$; ----, $m = 3$; ········, $m = 4$.

mode m	$-f_r$ (es)	$-f_i$ (es)	$-f_r$ (rp)
2	-0.1649	-0.1453×10^{-2}	—
3	-0.1779	-0.3319×10^{-4}	-0.181
4	-0.3439	-0.1531×10^{-3}	$+0.267$

TABLE 4. Eigenfrequencies for counter-rotating waves for cosine-transition vorticity basic state with $M = 1.5$, $\delta' = 1.0$ (es = eigenvalue shooting method, rp = random initial perturbations)

mode m	$-f_r$ (es)	$-f_i$ (es)	$-f_r$ (rp)
2	—	—	—
3	-0.02160	$-0.1625 \times 10^{-9}*$	-0.018
4	-0.11724	$-0.5408 \times 10^{-8}*$	—
4	$+0.58032$	$-0.8039 \times 10^{-6}*$	$+0.583$

TABLE 5. Eigenfrequencies for corotating and counter-rotating waves for Gaussian vorticity basic state with $M = 1.5$ (es = eigenvalue shooting method, rp = random initial perturbations; *, the differences in these decay rates are probably within convergence error)

positive f_r. Converged eigenfrequencies corresponding to counter-rotating waves that are very weakly decaying are then found (see table 4) for $m = 3$ as well as for $m = 2$ and 4.

Although figure 10(*a*) seems to indicate that there is a practically neutrally stable $m = 4$ mode which rotates in the same direction as the vortex, convergence to a corresponding solution was not obtained by the shooting method.

The results of §3.3 suggest that the Gaussian profile is neutrally stable for $m = 2$ normal modes. Here, the long-time behaviour of random perturbations is investigated for $M = 1.5$ with the $m = 2, 3, 4$ modes excited. This will confirm whether algebraically growing modes exist.

Plots of the log of the amplitude are given in figure 11(*a*, *b*). The growth rates for all three of the excited modes appear to be practically zero. The frequency for $m = 2$ also appears to be zero. For $m = 3$ and 4, a counter-rotating wave and a corotating wave are found respectively. Now, returning to the eigenvalue shooting code and using these results as initial guesses, counter-rotating waves for $m = 3, 4$ and a corotating wave for $m = 4$ are obtained (see table 5). The differences in the very small decay rates obtained by the shooting method are probably within convergence error.

5. Nonlinear development of perturbations

It is natural to ask what the fate of the vortex is in the nonlinear regime: will it continue to elongate unabated, reach an equilibrium state or undergo secondary instabilities? In this section, nonlinear behaviour is investigated via numerical solution of the two-dimensional Euler equations.

5.1. *Numerical method*

For convenience, the dimensional forms of the variables are used in the equations presented in this section. All variables are still normalized in the same manner as for the basic state variables in §2.1 (see (2.4)) and normalized variables are used in all the figures.

The two-dimensional Euler equations in full conservation law form in polar coordinates in an inertial reference frame are

$$\frac{\partial \boldsymbol{Q}}{\partial t}+\frac{\partial \boldsymbol{G}_r}{\partial r}+\frac{1}{r}\frac{\partial \boldsymbol{G}_\theta}{\partial \theta}+\boldsymbol{S}=0, \tag{5.1a}$$

where

$$\boldsymbol{Q}=\begin{bmatrix}\rho\\ \rho v_r\\ \rho v_\theta\\ e\end{bmatrix},\quad \boldsymbol{G}_r=\begin{bmatrix}\rho v_r\\ \rho v_r^2+p\\ \rho v_r v_\theta\\ v_r(e+p)\end{bmatrix},\quad \boldsymbol{G}_\theta=\begin{bmatrix}\rho v_\theta\\ \rho v_r v_\theta\\ \rho v_\theta^2+p\\ v_\theta(e+p)\end{bmatrix},\quad \boldsymbol{S}=\begin{bmatrix}\dfrac{\rho v_r}{r}\\ \dfrac{\rho}{r}(v_r^2-v_\theta^2)\\ \dfrac{2\rho v_r v_\theta}{r}\\ \dfrac{v_r}{r}(e+p)\end{bmatrix}, \tag{5.1b}$$

all the symbols have the same meaning as in §2.1 and e is the total energy per unit volume. The conservation law form of the Euler equations is employed in order to capture shocks accurately.

In the circumferential direction, fourth-order central-differencing is used on the flux vector $\boldsymbol{G}_\theta$. A Padé filter (Lele 1992) is applied in this direction every N_f steps to control the nonlinear build-up of high wavenumber errors. Let q_j be an element of $\boldsymbol{Q}$ at grid point j where j is counted periodically on the mesh. Then the filtered values $\check{q}_j$ are given by

$$\check{q}_{j-1}+A_f\check{q}_j+\check{q}_{j+1}=b_0 q_j+b_1(q_{j-1}+q_{j+1})+b_2(q_{j-2}+q_{j+2}), \tag{5.2a}$$

where

$$b_0=\tfrac{1}{4}(\tfrac{5}{2}A_f+3),\quad b_1=\tfrac{1}{2}(\tfrac{1}{2}A_f+1),\quad b_2=\tfrac{1}{8}(1-\tfrac{1}{2}A_f). \tag{5.2b}$$

The parameter A_f controls the cutoff wavenumber while the parameter N_f controls the amount of filtering. The ranges for A_f and N_f are $2.1 \leqslant A_f \leqslant 3.0$ and $50 \leqslant N_f \leqslant 100$ respectively.

In the radial direction, the Steger & Warming (1981) flux-splitting scheme is employed, which requires one-sided differencing and no artificial dissipation. The radial flux derivative in (5.1*a*) is replaced by

$$\delta_r \boldsymbol{G}_r=\delta_r^b \boldsymbol{G}_r^+ +\delta_r^f \boldsymbol{G}_r^-, \tag{5.3}$$

where δ_r^b and δ_r^f are third-order upwind biased difference operators in r defined by (4.10*c*) and

$$\boldsymbol{G}_r^\pm \equiv \frac{\rho}{2\gamma}\begin{bmatrix}2g_m\lambda_1^\pm+\lambda_3^\pm+\lambda_4^\pm\\ 2g_m\lambda_1^\pm v_r+\lambda_3^\pm(v_r+c)+\lambda_4^\pm(v_r-c)\\ 2g_m\lambda_1^\pm v_\theta+\lambda_3^\pm v_\theta+\lambda_4^\pm v_\theta\\ g_m\lambda_1^\pm(v_r^2+v_\theta^2)+\tfrac{1}{2}\lambda_3^\pm[(v_r+c)^2+v_\theta^2]+\tfrac{1}{2}\lambda_4^\pm[(v_r-c)^2+v_\theta^2]+w\end{bmatrix}, \tag{5.4}$$

initial amplitude	$-f_r$	$-f_i$
*	0.8201	0.01243
0.005	0.8200	0.01228
0.01	0.8200	0.01227
0.05	0.8199	0.01203

TABLE 6. Frequencies and growth rates for $M = 1.5$ at small time with different initial perturbation-amplitudes (*, results of linear stability analysis)

where $g_m \equiv (\gamma - 1)$, $w \equiv (3-\gamma)(\lambda_3^{\pm} + \lambda_4^{\pm})\, c^2/(2g_m)$, $\lambda_i^{\pm} = \frac{1}{2}(\lambda_i \pm |\lambda_i|)$ and $\lambda_1 = v_r$, $\lambda_3 = v_r + c$, $\lambda_4 = v_r - c$ are the eigenvalues of the flux Jacobian matrix $\boldsymbol{A}_r$ of $\boldsymbol{G}_r$. The flux vectors $\boldsymbol{G}_r^{\pm}$ above are formed from $\boldsymbol{G}_r^{\pm} = \boldsymbol{A}_r^{\pm} \boldsymbol{Q}$ where $\boldsymbol{A}_r^{\pm} = \boldsymbol{X}_r \boldsymbol{\Lambda}_r^{\pm} \boldsymbol{X}_r^{-1}$ with $\boldsymbol{X}_r$ being the eigenvector matrix of $\boldsymbol{A}_r$, and $\boldsymbol{\Lambda}_r^{\pm}$ are diagonal matrices with λ_i^+ and λ_i^- as their elements, respectively.

The time-advance scheme is RK3 as in §4. The initial condition consists of the basic state for the cosine-transition vorticity profile with $\delta' = 1$ and $M = 1.5$ plus the $m = 2$ eigenfunctions from the normal-mode analysis.

Since an $m = 0$ mode (purely radial variations) may be generated by nonlinear interactions, the flow variables must be updated in time at the origin. This is accomplished by locally solving the Cartesian form of the equations using central differencing on a five-point 'cross' stencil centred at the origin, with the surrounding four points located at the first $r =$ const. grid line. The velocity components should remain zero at the origin due to symmetry, and this was verified to be so.

The basic state does not satisfy the finite-difference equations exactly nor the numerical boundary conditions. Although these errors are initially small, they generate perturbations that are amplified at each time step. These errors were reduced to a negligible level by subtracting out the finite difference operator acting on the basic state from the difference equations.

It was pointed out to us (K. W. Thompson, personal communication) that the treatment of the far-field boundary by the non-reflective condition of Thompson (1987) does not preserve the steady basic state in time. This is because the 'in-coming parts' of the characteristic variables are set to zero by the Thompson condition, resulting in a loss of balance of radial momentum. The error will propagate inwards and contaminate the interior solution. This problem was remedied by adding the appropriate terms for the 'in-coming part' of the basic-state characteristic variables such that radial momentum balance is restored (see Appendix).

5.2. *Validation of the method*

A (64 × 139) polar mesh with 64 points in the circumferential direction and 139 points in the radial direction is used. The initial behaviour of the $m = 2$ mode is found to agree with the prediction of linear theory at several Mach numbers. As examples, the frequencies and growth rates at $M = 1.5$ are given in table 6 for three different initial perturbation amplitudes. As expected, deviation from the normal-mode solution increases as the perturbation amplitude increases.

Nonlinear terms are not the only cause of deviation from linear theory. The presence of the Padé filter also results in a slight departure ($\approx 0.6\,\%$). Practically identical results for the linear behaviour are obtained by placing the far-field boundary at $x = 20$ and $x = 40$.

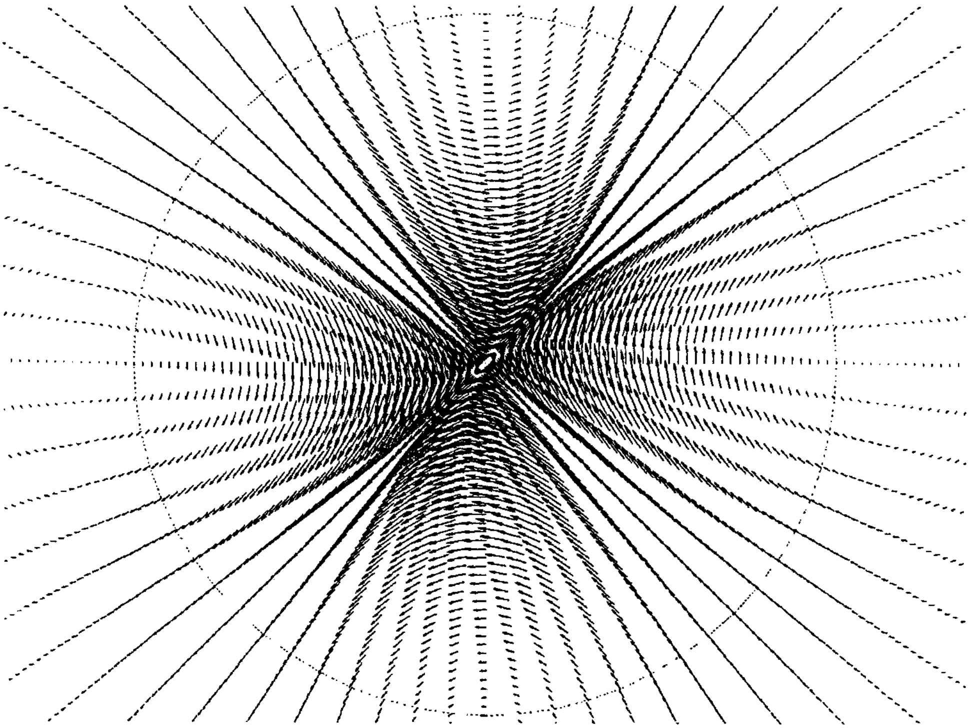

FIGURE 12. Perturbation-velocity field at $t = 0$; dotted circle indicates $x = 1$.

5.3. *Results of nonlinear simulations*

With the robustness and accuracy of the Euler code established, numerical experiments can now be performed with the insight gained to guide the choice of numerical parameters. In order to reach the nonlinear regime reasonably quickly, a fairly large initial perturbation amplitude of 0.05 is used. The results described below are for a (192×197) polar mesh with the far-field boundary at $x = 20$. Qualitatively similar results are obtained for a (128×197) mesh. Also, a (64×139) mesh gives similar results except that the angular phase velocities of perturbation Fourier modes for the radial velocity decay faster in time than with the finer meshes.

5.3.1. *Evolution of the perturbed vortex*

First it is instructive to consider the situation at $t = 0$. Near the vortex centre, the perturbation-velocity field is like a straining field (figure 12) while the total vorticity ω_z contours are approximately elliptical in shape and the vorticity is non-zero in the region $x \leqslant 1.5$ (figure 13). Since the density contours are approximately circular, the ω_z/ρ contours are also elliptical. The vorticity equation is

$$\frac{\mathrm{D}}{\mathrm{D}t}\left(\frac{\omega_z}{\rho}\right) = \frac{\nabla T \times \nabla S}{\rho}. \tag{5.5}$$

For a homentropic basic state, it can be shown from the linearized equations that the

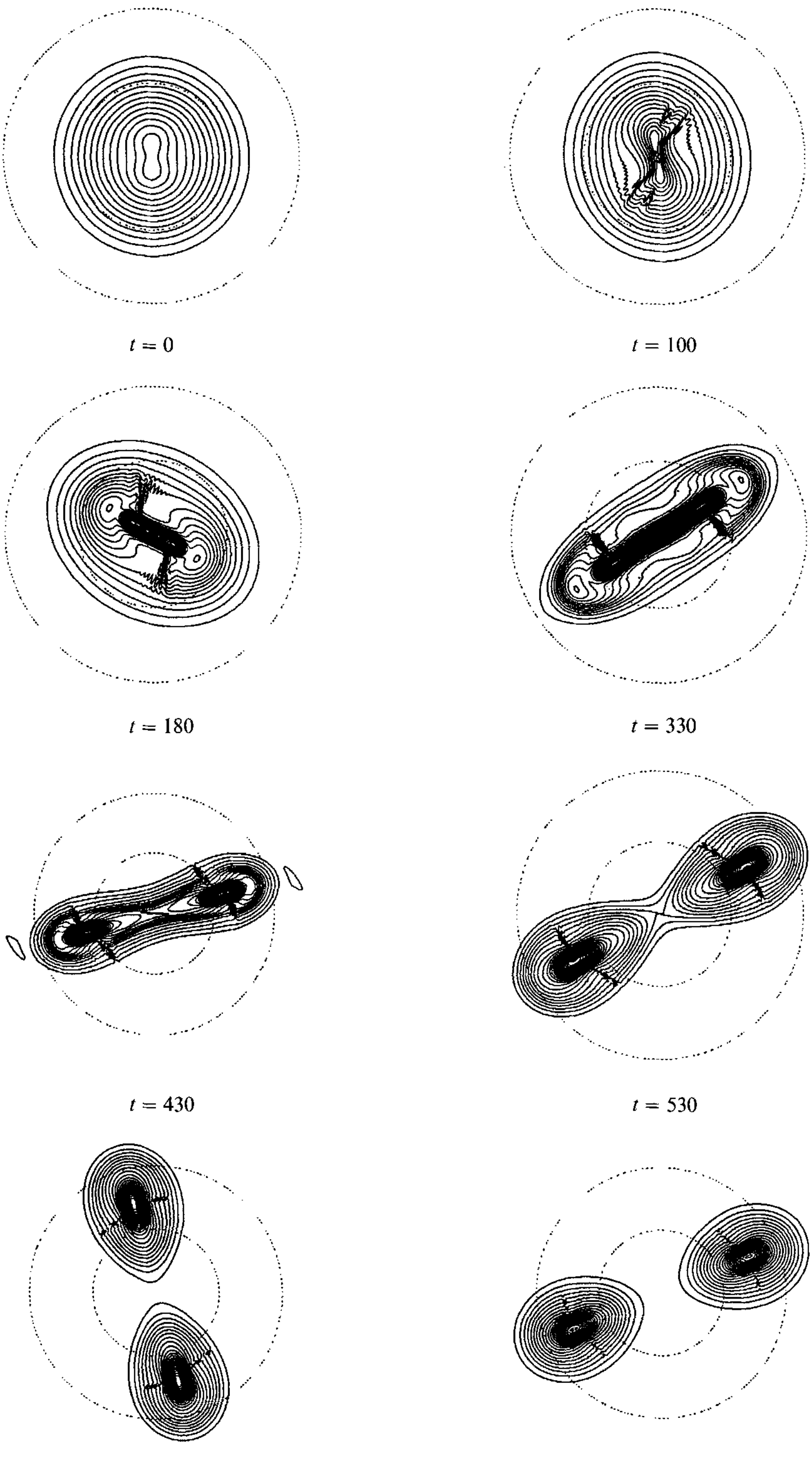

$t = 0$ $t = 100$

$t = 180$ $t = 330$

$t = 430$ $t = 530$

$t = 630$ $t = 730$

FIGURE 13. Normalized vorticity contours (min. = 0, max. = 10.25, increment = 0.25). Dotted circles indicate $x = 1$ and $x = 2$, and positive vorticity is out of the plane of the paper.

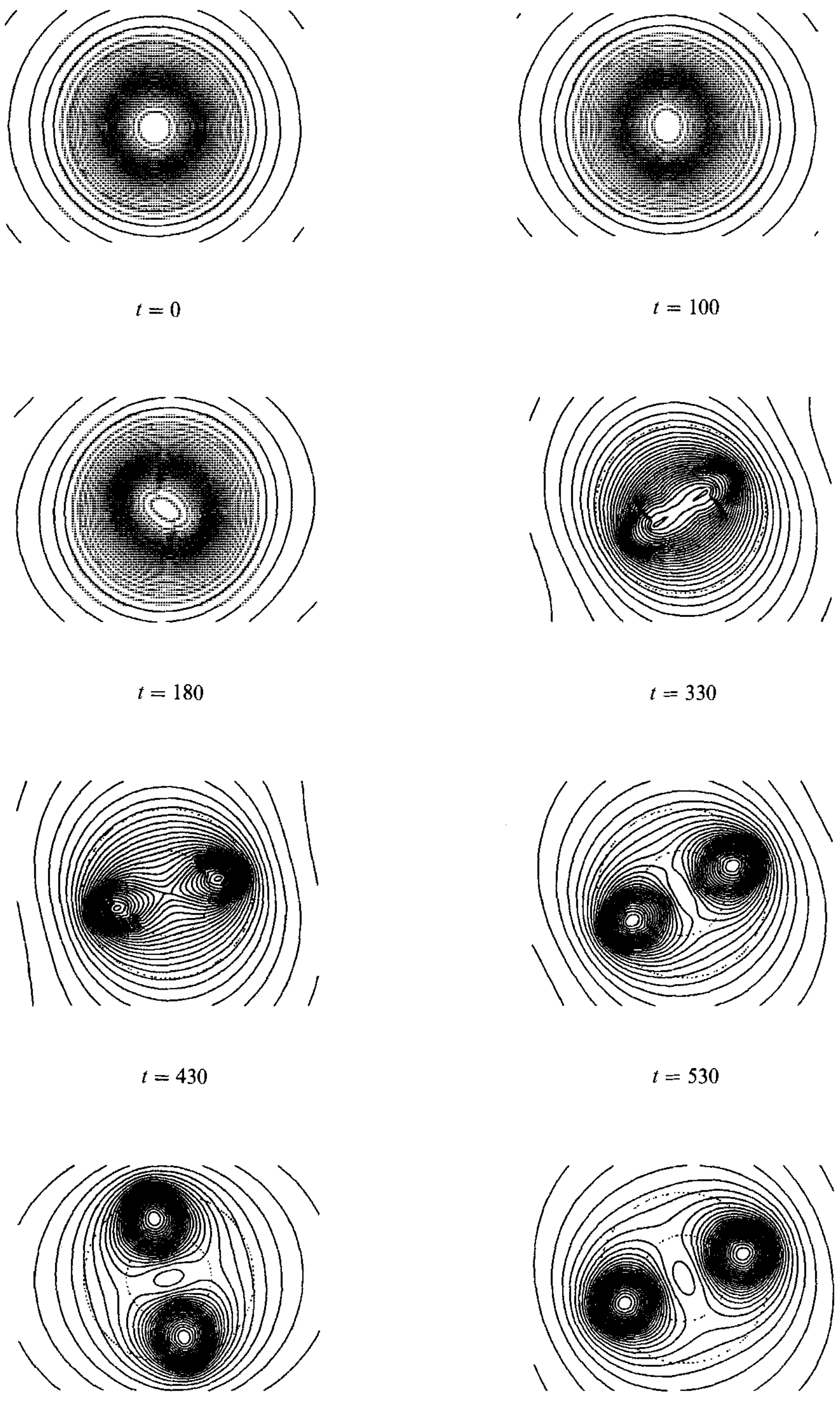

$t = 0$

$t = 100$

$t = 180$

$t = 330$

$t = 430$

$t = 530$

$t = 630$

$t = 730$

FIGURE 14. Normalized density contours (min. = 0, max. = 3.4, increment = 0.1). Dotted circles indicate $x = 1$ and $x = 2$.

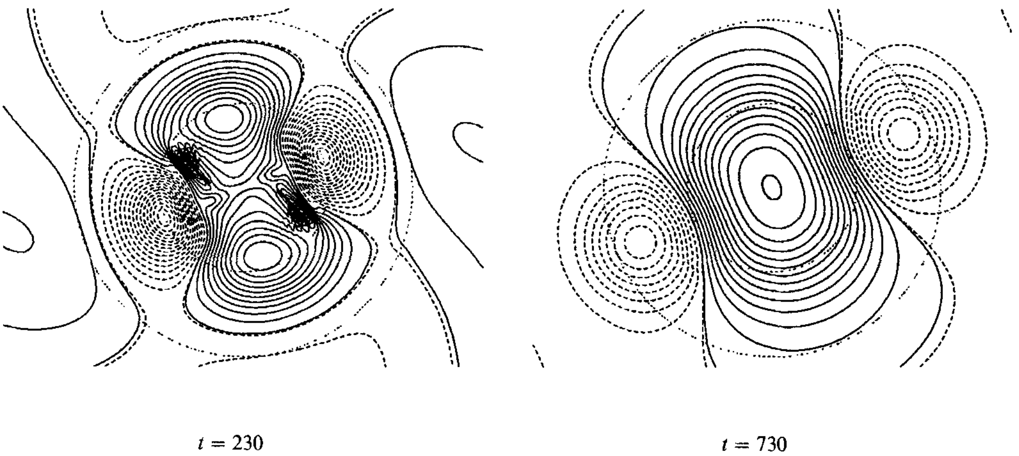

FIGURE 15. Normalized perturbation density contours: ----, negative values; ——, positive values; dotted circles indicate $x = 1$ and $x = 2$. At $t = 230$, min. $= -0.30$, max. $= 0.22$, inc. $= 0.02$; at $t = 730$, min. $= -1.8$, max. $= 2.7$, inc. $= 0.2$.

entropy perturbation is second order. Hence the term on the right-hand side of (5.5) is zero to first order. This implies that ω_z/ρ contours are convected by the local velocity, which consists of the basic state and the perturbation. Convection by the basic state results in circular motion about the origin while that by the perturbation is like a strain. The axis of strain is at approximately 45° to the major axis of the elliptical ω_z/ρ contours, which is not favourable for elongation of the vortex. This is consistent with the slow growth of the perturbations in the initial linear regime. If the axis of strain and the major axis of the elliptical vorticity contours were aligned, the elongation would be much faster and the subsequent behaviour would be very different.

The evolution of vorticity and density in the region $0 \leqslant x \leqslant 2$ is plotted in figures 13 and 14. The eddy turnover time based on the normalized maximum tangential velocity is $t_e = 2\pi$. The evolution of the vortex can be divided into three main stages. The first is the linear regime. After $t \approx 20$, which marks the beginning of the second stage, more significant nonlinear interactions can be observed. The core becomes more elliptical and the vorticity near the centre intensifies. The core continues to elongate until the vortex splits into two corotating vortices after $t \approx 350$, which marks the end of the second stage. During the third stage, the vortices gradually move away from each other.

Viscous effects during the simulation can be neglected provided the time of the run $\tau_{\text{run}} \ll a^2/\nu$, where a is the reference radial dimension of the vortex and ν is the kinematic viscosity, or $Re \equiv a\bar{V}_\theta(a)/\nu \gg \tau_{\text{run}}\bar{V}_\theta(a)/a$. For the run described above, $\tau_{\text{run}}\bar{V}_\theta(a)/a$ is 760, while typical values of Re for vortices found in high-speed aerodynamic flows range from 10^4 to 10^5 (Dosanjh & Weeks 1965; Mandella 1987).

Now the stages of the evolution after the linear regime are considered in more detail. One of the first effects of nonlinearity is the steepening of gradients near the ends of the elliptical core. These develop into weak shocklets at later times (the entropy change across them is small). This steepening is analogous to the steepening of compression waves in the one-dimensional equations of motion (Liepmann & Roshko 1957, §3.10). However, this analogy cannot be taken too far since the flow here contains significant radial variations.

During the elongation stage, the maximum Mach number in the flow increases slowly (up to about 1.9) until splitting occurs ($t \approx 350$). The density contours are

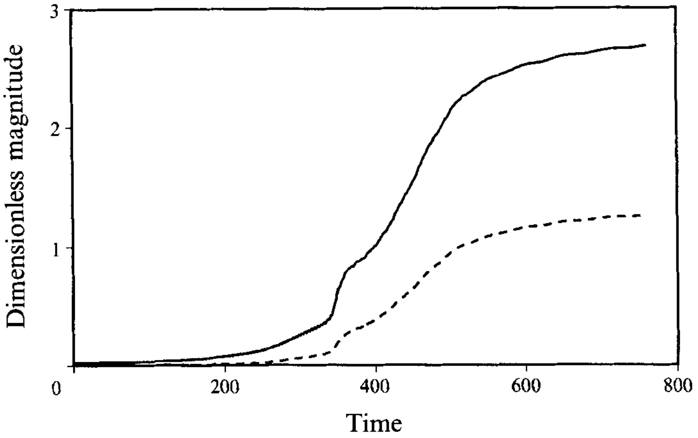

FIGURE 16. Variations of normalized density and pressure at the origin: ——, density; – – – –, pressure.

almost circular initially. As the nonlinearity develops, small kinks appear that correspond to the steepening of the gradients (see figure 14); in figure 15, the $t = 230$ plot indicates that the steep gradients lie in the regions of positive perturbation density. The density and pressure at the centre of the vortex increase with time (see figure 16) and after $t = 430$ a region of high density is formed about the origin. This is due to the action of the nonlinearly generated $m = 0$ mode that results in a net mass inflow near the vortex centre. This process is eventually accompanied by splitting. The vortex core gradually becomes more elliptical and then splits into two corotating vortices. The splitting of an inviscid incompressible vortex with an elliptical constant-vorticity core into two corotating vortices in an unbounded fluid has been observed in nonlinear calculations by Dritschel (1986). The linear-stability analysis by Love (1893) for this vortex indicates that it is unstable to a splitting mode ($n = 4$ in elliptic coordinates) for aspect ratios greater than ≈ 4.75. The rapid splitting observed in the present numerical simulations may be a similar inertial phenomenon. In the analysis by Love, the $n = 3$ (filamentation) mode is the first to become unstable at an aspect ratio of three. In the present case, since only the $m = 2$ mode is excited initially, only even modes are nonlinearly generated, and a potential instability of the $n = 3$ mode may be suppressed for that reason.

After splitting occurs, the maximum Mach number decreases (down to about 1.0 at $t = 730$). Immediately after the splitting, each of the vortices is elliptical in shape with new regions of steep gradients present at opposite ends inside each of the split vortices (see figure 13 at $t = 430$). The gradients gradually become less steep as the vortices move apart and the flow around each vortex becomes more circular. The density deficits in the split vortex cores relative to the far field are much less than that of the original vortex. The perturbation-density contour plot at $t = 730$ in figure 15 indicates that mass continues to move into the region around the origin after splitting occurs.

As the vortices move away from the origin, their rate of rotation about the origin decreases. Two inviscid incompressible point vortices of strength Γ rotate with angular velocity

$$\dot{\phi}_p = \Gamma/(8\pi d_s^2), \tag{5.6}$$

where d_s is the half-separation distance. The numerically obtained rotation rate $\dot{\phi}$ of the split vortices in the present case is compared with this expression in figure 17(*a*).

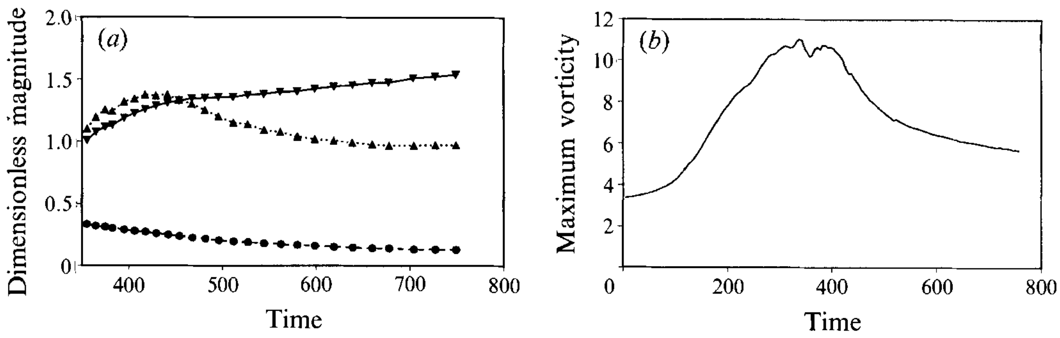

FIGURE 17. (a) Comparison of rotation rate of split vortices $\dot{\phi}$ about origin with the value $\dot{\phi}_p$ for co-rotating point vortices: —▼—, normalized half-separation distance ≡ d_s; ---●---, $\dot{\phi}$; ···▲···, $\dot{\phi}/\dot{\phi}_p$. (b) Normalized maximum vorticity.

The plot shows that as the split vortices move further away from each other, the velocities that they induce on each other are more like those of point vortices, i.e. $\dot{\phi}/\dot{\phi}_p$ tends to unity with time. Figure 17(b) shows the behaviour of the peak vorticity. It is located at the origin during the elongation phase. Since a fluid particle started at the origin remains there, the value of ω_z/ρ at the origin must be nearly constant in this nearly homentropic flow. Hence increase of ω_z is associated with increase of ρ (see figure 16). In the drifting apart phase, the peak vorticity, located in the cores of the split vortices, decreases in time. The value of the minimum density in the core increases, however, suggesting that the vorticity peak and density minimum occur for different fluid particles.

5.3.2. *Evolution of Fourier modes*

Unlike the linear regime, the nonlinear behaviour of the flow is highly influenced by the local amplitude of the perturbations. This is expected to be strongest near $x = 0.4$ where the eigenfunctions for two of the variables have their global maxima. Since the normal-mode assumption is no longer valid, different locations of the flow field may now behave differently. However, the frequencies and growth rates can still be analysed at different radial locations in the same manner as for the linear theory for purposes of comparison. Since the initial condition contains only an $m = 2$ mode, odd modes cannot be produced from nonlinear interaction, and their amplitudes in the numerical solution are found to be negligible compared to the even modes.

The logs of the leading even-Fourier-mode amplitudes for v_r at $x = 0.8$ are shown in figure 18(a) (for normal modes, the growth rates would be given by the slopes). A weak $m = 0$ mode is also present as a result of the $m = 2$ mode self-interaction. The plot shows that the growth rates decrease gradually in the nonlinear regime until they approach saturation just before splitting occurs. After splitting, all the Fourier modes in the location of the former vortex core ($0 \leqslant x \leqslant 1.5$) start to decay as the split vortices move away from the origin.

The angular phase velocities $-f_r/m$ of the leading Fourier modes at $x = 0.8$ are plotted in figure 18(b) (very similar results are obtained at the other locations). After a brief period of excitation, the $m = 4$ and 6 modes have the same angular phase velocity as the $m = 2$ mode, i.e. the waves do not disperse. On the other hand, the angular phase velocities of linear waves on a circular incompressible uniform-vorticity vortex are given by $(m-1)/m$, i.e. they do depend on m. In the present case, the waves do not show this behaviour because they are forced by the $m = 2$ mode. The rotation

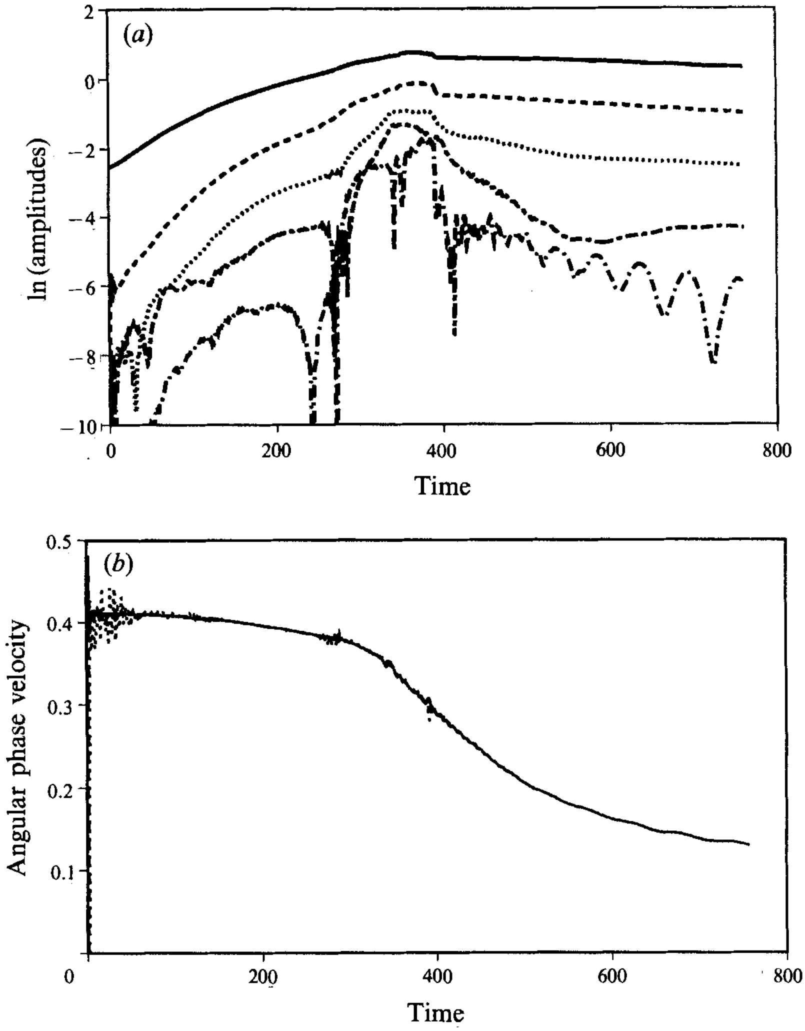

FIGURE 18. (a) Natural log of Fourier mode amplitudes for $m = 0, 2, 4, 6, 8$ and (b) angular phase-velocities of Fourier modes $m = 2, 4, 6$, for v_r at $x = 0.8$: ——, $m = 2$; – – – –, $m = 4$; ········, $m = 6$; – – – –, $m = 8$; —·—, $m = 0$.

rate of the waves decreases slightly during the elongation stage. This is analogous to the fact that more elongated Kirchhoff's elliptic vortices (incompressible flow with constant-vorticity core) have smaller rotation rates according to $\bar{\omega}_0 \lambda/(\lambda+1)^2$, where $\bar{\omega}_0$ is the uniform value of vorticity in the core and λ is the aspect ratio (see Lamb 1932, §159). A sharper decrease in the rotation rate of the waves is observed subsequent to the split.

5.3.3. *Acoustic radiation*

The instantaneous acoustic power E_r (per unit length) at a radial distance r_a is given by

$$E_r = \int_0^{2\pi} r_a \tilde{p} \tilde{v}_r \,\mathrm{d}\theta, \tag{5.7}$$

where $\tilde{p}$ and $\tilde{v}_r$ are the perturbation pressure and radial velocity, respectively. The

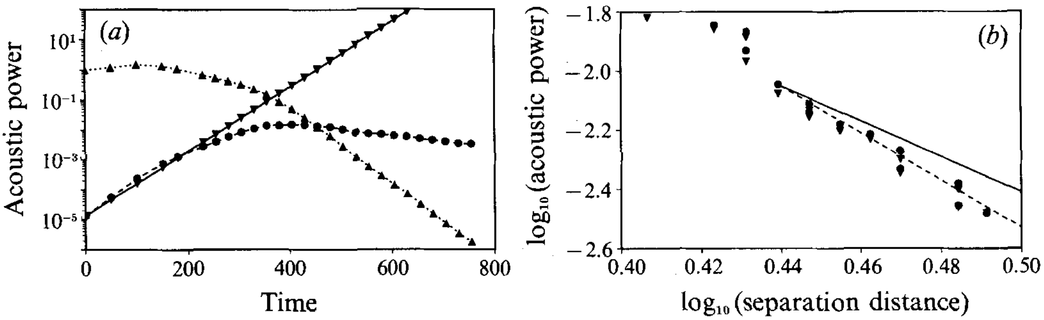

FIGURE 19. (*a*) Comparison of normalized acoustic power at $x = 10$ between linear theory and Euler simulation: —▼—, linear theory; ---●---, Euler; ···▲···, Euler/linear ratio. (*b*) Variation of normalized far-field acoustic power with vortex separation distance: ▼, $x = 10$; ●, $x = 15$; ——, slope $= -6$; ----, slope $= -8$.

normalized acoustic power at $x = 10$ is compared with linear theory in figure 19(*a*). The nonlinear Euler simulation shows good agreement with linear theory in the initial small-amplitude phase as expected. As the nonlinearity becomes stronger, the acoustic power first increases with time, then decreases. The acoustic power reaches a maximum at about the time when the vortex starts to split.

An analytic expression for the acoustic power of two corotating point vortices in an inviscid fluid at small Mach numbers is given in Müller & Obermeier (1967). Their analysis predicts that the acoustic power should be inversely proportional to the separation distance of the two vortices to the sixth power. The Mach number, M_{rot}, based on the rotation speed of the vortices about each other and the ambient sound speed, is about 0.2 at the end of the simulation. For aeroacoustic theories to be valid, the compactness condition that the ratio of the acoustic wavelength to the half-separation distance of the vortices be very large must be satisfied. This ratio equals 15.7 at the end of the simulation, which implies that the compactness condition may be only marginally satisfied.

Figure 19(*b*) shows the log of the acoustic power at $x = 10$ against the log of the separation distance. In some cases there are two values of acoustic power for a given separation distance due to small oscillations of the location of the centres of the individual vortices from one grid point to the next. The approximate slope of the plot suggests an inverse eighth-power variation with separation distance. This result has to be interpreted with some caution since only a small range of separation distance on the log scale is available in the flow. The discrepancy with the theory for point vortices may be due to several sources. First, the acoustic relations

$$p' = c_\infty^2 \rho', \quad p' = \pm \frac{\gamma p_\infty}{c_\infty} v_r' \qquad (5.8a, b)$$

at $x = 10$ are not satisfied exactly. Figure 20(*a*) shows that the perturbation pressure and perturbation density follow the small-disturbance isentropic relation throughout the simulation. However, figure 20(*b*) reveals that there is deviation of the perturbation pressure and radial-velocity relation from (5.8*b*) after $t \approx 150$. The second reason for the discrepancy is that the theory describes only the acoustic signal produced by the corotation of the point vortices. Since the vortices are of finite sizes in the present case, the unsteadiness of each individual core also contributes to the acoustic power. Because the separation distance between the cores is comparable to the core size, the characteristic frequencies for both forms of unsteadiness are also comparable. Hence,

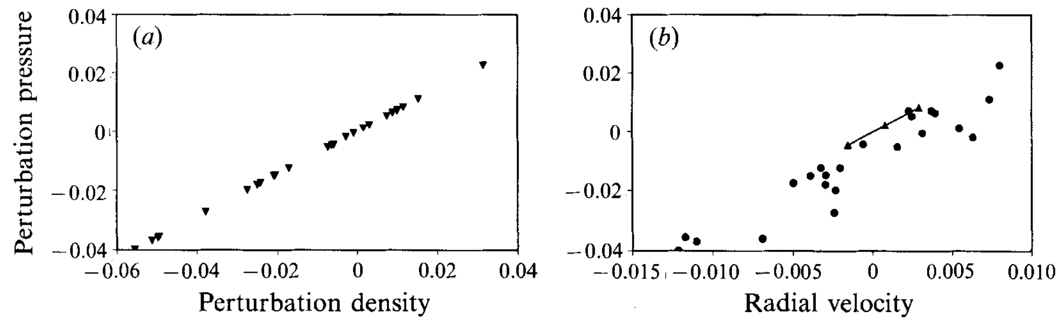

FIGURE 20. (*a*) Normalized perturbation pressure and perturbation density relation, and (*b*) normalized perturbation pressure and radial velocity relation sampled at different times at $x = 10$: ▼, all t; —▲—, $t < 150$; ●, $t > 150$.

it is difficult to separate the two contributions to the acoustic power. Another source of discrepancy may be that the acoustic signal is not captured accurately due to the relatively coarse resolution of the mesh in the far field. A study of many issues concerning the accurate computation of acoustic waves for a pair of corotating vortices was recently performed by Mitchell, Lele & Moin (1992).

5.3.4. *Behaviour of total mass, energy, circulation and entropy*

Both the total mass and energy in the computational domain show a very small loss of less than 1% of the initial value, which is quite satisfactory considering the large number of time steps used (≈ 700000). The slight decrease in total mass is expected since the flow develops a small net outflow. The slight reduction in total energy can be accounted for by energy carried out with the small mass outflow and the escape of acoustic radiation. For both quantities, small numerical errors also contribute to the loss. A small increase of total circulation in the computational domain is observed due to production by the baroclinic term and contributions from the numerical boundary conditions at the far field.

For an inviscid fluid in the absence of shocks, redistribution of entropy is allowed but the maximum should remain the same. The initial condition for the present numerical simulation is very slightly non-homentropic (less than ≈ 0.1% from a constant) because the perturbation eigenfunctions are only homentropic up to linear terms. The maximum value of entropy attained is about 50% greater than the initial value and most of the entropy is generated during the presence of high gradient regions (at the unsplit vortex core and at the weak shocklets). Near the vortex centre, the core has become so elongated that the flow resembles a shear layer locally with gradients that are comparable to those found in the shocklets. Part of the excess entropy may be due to inherent dissipation in the numerical scheme. Although the maximum entropy has increased quite significantly, the total entropy of the entire flow field remains within less than 0.1% of the initial value. This suggests that the effect of the local numerically produced entropy on the global behaviour of the flow is small. The effect of the numerical scheme on entropy generation has been examined by Brentner (1990). It was found that typical values of added artificial dissipation have negligible effect on entropy generation but poor grid resolution can produce significant errors in entropy production.

6. Summary and discussion

We have studied the linear and nonlinear instabilities of a compressible two-dimensional vortex. The main results are as follows.

(i) The linear instability is not peculiar to the previously studied case of uniform vorticity that jumps to zero at the core boundary. It is found that other smoother vorticity distributions are also unstable.

(ii) The Gaussian vorticity profile is found to have only neutrally stable modes according to a normal-mode stability analysis. In addition, a study of the linear initial-value problem indicated no algebraically growing modes either. Kop'ev & Leont'ev (1988) found that any continuous axisymmetric vorticity distribution whose gradient does not change sign provides a variational maximum for the energy, and concluded that all such profiles should be acoustically unstable. A possible reason for our observation of neutral stability of the Gaussian profile is that modes are non-radiating. Indeed it is possible that the $m = 2$ mode has zero frequency, i.e. it is steady (see figure 11 *a*). Unsteady modes can also be non-radiating if the eigenfunctions decay sufficiently rapidly with distance from the origin.

(iii) For a model entropy profile, positive average entropy gradient in r is destabilizing while the opposite is true for negative average entropy gradient.

(iv) A wave rotating in the direction opposite to the vortex was found in the long-time solution of the linear initial-value problem for random initial conditions. The wave was observed for $m = 3$ for the cosine transition profile and the Gaussian profile. Its existence was confirmed by returning to the normal-mode analysis. The normal-mode analysis then also revealed other counter-rotating waves, which were not observed in the random initial-value problem, presumably because they decay faster. All such modes encountered were either decaying or neutral.

(v) In the nonlinear development of an elliptic perturbation, the vortex elongates and shocklets are formed near the ends of the vortical core. After sufficient elongation, the vortex splits into two corotating vortices by a mechanism that we believe is inertial and the same as a Love (1893) instability of an incompressible Kirchhoff elliptic vortex. Each of the vortices has a density trough, while a region of high density is created about the origin.

We wish to comment, in passing, on the possible relevance of the behaviour observed here and the appearance of secondary structures in the experiments of Dosanjh & Weeks (1965). In the experiments, a spiral vortex was generated by passing a shock wave over an airfoil. Subsequent to interaction with the reflected shock, the vortex was distorted into an elliptical shape and evolved in essentially still air. We estimate that $M \approx 0.5$ and the eddy turnover time as 100 μs ($\equiv \tau_e$). About $30\tau_e$ after the interaction, a secondary region of high density appears and subsequently grows in strength and size (splitting occurs at about 50 eddy turnover times in the numerical simulation). The primary vortex decays in strength (decreasing density deficit) and a secondary vortex appears which grows in strength (increasing density deficit). The primary and secondary vortices are unequal in size and the high-density region does not lie between them, whereas the split vortices in the present numerical simulation are of equal size and strength with the high-density region located in between them. We believe that the above differences between the experiments and the numerical simulation are due to differences in initial condition, though it is possible that the splitting mechanisms are related.

In the final stage of the nonlinear development, the vortices drift apart. This phenomenon was predicted by Klyatskiy (1966) and is explained as follows. For incompressible flow, although the kinetic energy of the unbounded vortex system is infinite, one can define a finite quantity, the 'excess energy', which is the difference between the kinetic energy of a potential vortex with the same total vorticity, and the kinetic energy of the system (Batchelor 1967, §7.3). For two corotating incompressible point vortices, the 'excess energy' is proportional to $-\log(d_s)$, i.e. two vortices that are farther apart have a lower 'excess energy'. As acoustic energy is radiated out with slight compressibility, the system of corotating vortices must move to a lower energy state. A process which allows this is the drifting apart of the vortices. It would be worth seeking an argument for the separation based on the local evolution of the flow variables.

The authors are grateful to Dr Sanjiva Lele for some very helpful discussions, and to a referee for useful comments about relevant work in the geophysical literature. Funding for this work was provided by a NASA/Stanford consortium agreement (Contract number NCA2-361). Computer resources were supplied by NASA Ames Research Center.

Appendix. Modification and implementation of Thompson's non-reflective boundary condition at the far-field boundary

In the numerical simulation of the linear initial-value problem and the nonlinear problem, the non-reflective boundary condition of Thompson (1987) is used to promote outward propagation of acoustic waves at the far-field boundary. This is a valid scheme for this problem since variations tangential to the boundary are small. The scheme used to advance the flow in time in the interior is also used at the boundary. Derivatives tangential to the boundary (θ-derivatives) are computed in the same manner as for the interior while derivatives normal to the boundary (r-derivatives) are treated in a special way. The procedure used for the linear initial-value problem is a direct application of Thompson's scheme and the reader is referred to Chan (1990) for the details. The procedure used for the nonlinear problem is described below.

Let $U=[\rho, v_r, v_\theta, p]^{\mathrm{T}}$ be the vector of primitive variables and let terms in the conservative and primitive formulations be related by

$$\frac{\partial Q}{\partial t}=\boldsymbol{P}\frac{\partial U}{\partial t}, \qquad \frac{\partial G_r}{\partial r}=\boldsymbol{R}\frac{\partial U}{\partial r}, \tag{A 1}$$

with Q and G_r as defined in (5.1 a, b). Defining $\boldsymbol{A}\equiv \boldsymbol{P}^{-1}\boldsymbol{R}$, the radial flux derivative in (5.1 a) can be written as

$$\frac{\partial G_r}{\partial r}=\boldsymbol{PA}\frac{\partial U}{\partial r}=\boldsymbol{PT}^{-1}\left(\Lambda \boldsymbol{T}\frac{\partial U}{\partial r}\right), \tag{A 2}$$

where the columns of $\boldsymbol{T}^{-1}$ are the right eigenvectors of $\boldsymbol{A}$, and Λ is the diagonal matrix of eigenvalues λ_i of $\boldsymbol{A}$. Let $\boldsymbol{M}$ denote the factor in parentheses and let $\boldsymbol{l}_k^{\mathrm{T}}, k=1,\ldots,4$ denote the rows of $\boldsymbol{T}$. Then the kth element of $\boldsymbol{M}$ is

$$M_k=\lambda_k \boldsymbol{l}_k^{\mathrm{T}}\frac{\partial U}{\partial r}. \tag{A 3}$$

Thompson's procedure requires setting $M_k=0$ for $\lambda_k<0$, which suppresses incoming waves for a constant-coefficient, one-dimensional linear system. After expanding (A 3), replacing derivatives by backward differences and applying Thompson's procedure, one obtains

$$\left.\begin{aligned} M_1 &= \begin{cases} (v_r-c)[\delta_r^b p-\rho c\delta_r^b v_r] & \text{for } (v_r-c)>0,\\ 0 & \text{otherwise,}\end{cases}\\ M_2 &= \begin{cases} v_r\delta_r^b v_\theta & \text{for } v_r>0,\\ 0 & \text{otherwise,}\end{cases}\\ M_3 &= \begin{cases} v_r[\delta_r^b p-c^2\delta_r^b \rho] & \text{for } v_r>0,\\ 0 & \text{otherwise,}\end{cases}\\ M_4 &= \begin{cases} (v_r+c)[\delta_r^b p+\rho c\delta_r^b v_r] & \text{for } (v_r+c)>0,\\ 0 & \text{otherwise.}\end{cases}\end{aligned}\right\} \tag{A 4}$$

For radial momentum balance, we consider the second element of the radial flux derivative, which can be expressed as

$$\left(\frac{\partial G_r}{\partial r}\right)_2 = \frac{1}{2c}(M_4-M_1)-\frac{v_r}{c^2}(M_3-\tfrac{1}{2}(M_1+M_4)). \tag{A 5}$$

For the basic-state, $v_r = 0$ and hence $M_1 = 0$ and $M_4 = \bar{c}\delta_r^b\bar{p}$ such that $(\partial G_r/\partial r)_2 = \frac{1}{2}\delta_r^b\bar{p}$ instead of the value $\mathrm{d}\bar{p}/\mathrm{d}r$ needed to balance $\rho\bar{V}_\theta^2/r$ in S for satisfaction of the radial momentum equation (K. W. Thompson, personal communication). This error will propagate inwards and contaminate the interior solution, resulting in the generation of a non-zero radial-velocity component. By adding appropriate terms for the 'incoming' parts of M_1 and M_4, radial-momentum balance for the basic state is restored (K. W. Thompson, personal communication). However, the resulting radial-momentum equation is still not satisfied exactly due to truncation errors in computing $\delta_r^b p$ by finite differences. This error is eliminated by adding two terms to the outgoing parts of M_1 and M_4. Since these terms sum to zero analytically, the conceptual basis of Thompson's scheme is not altered. The re-defined M_1 and M_4 are as follows:

$$\left.\begin{aligned} M_1 &= \begin{cases} (v_r-c)\,[\bar{\rho}\bar{V}_\theta^2/r+\delta_r^b(p-\bar{p})-\rho c\delta_r^b v_r] & \text{for } (v_r-c)>0,\\ (v_r-c)\bar{\rho}\bar{V}_\theta^2/r & \text{otherwise,}\end{cases}\\ M_4 &= \begin{cases} (v_r+c)\,[\bar{\rho}\bar{V}_\theta^2/r+\delta_r^b(p-\bar{p})+\rho c\delta_r^b v_r] & \text{for } (v_r+c)>0,\\ (v_r+c)\bar{\rho}\bar{V}_\theta^2/r & \text{otherwise.}\end{cases}\end{aligned}\right\} \tag{A 6}$$

With (A 6) and M_2 and M_3 as defined in (A 4), the steady basic-state is maintained by the numerical simulations (up to round-off error). Also, since we saw no evidence of reflections from the far-field boundary, we concluded that the character of Thompson's scheme does not seem to be affected by the modifications needed to maintain the basic state. However, users of Thompson's scheme must take care in checking if any correction needs to be applied to the scheme for use in a flow with a non-uniform basic state.

REFERENCES

Batchelor, G. K. 1967 *An Introduction to Fluid Dynamics*. Cambridge University Press.

Brentner, K. S. 1990 The sound of moving bodies. PhD dissertation, Cambridge University.

Broadbent, E. G. 1976 Jet noise radiation from discrete vortices. *Aero Res. Counc. R.&M.* 3826.

Broadbent, E. G. 1984 Stability of a compressible two-dimensional vortex under a three-dimensional perturbation. *Proc. R. Soc. Lond.* A **392**, 279–299.

Broadbent, E. G. & Moore, D. W. 1979 Acoustic destabilization of vortices. *Phil. Trans. R. Soc. Lond.* A **290**, 353–371.

CHAKRAVARTHY, S. R. 1979 The split coefficient matrix method for hyperbolic systems of gasdynamic equations. PhD dissertation, Iowa State University.

CHAN, W. M. 1990 Instabilities of two-dimensional inviscid compressible vortices. PhD dissertation, Stanford University.

CHEN, J. H., CANTWELL, B. J. & MANSOUR, N. N. 1989 The effect of Mach number on the stability of a plane supersonic wake. *AIAA Paper* 89-0285.

COLONIUS, T., LELE, S. K. & MOIN, P. 1991 The free compressible viscous vortex. *J. Fluid Mech.* **230**, 45–73.

CRIGHTON, D. G. & WILLIAMS, J. S. 1993 Nonlinear theory of the Broadbent–Moore compressible vortex instability. *J. Fluid Mech.* (submitted).

DOSANJH, D. S. & WEEKS, T. M. 1965 Interaction of a starting vortex as well as a vortex sheet with a traveling shock wave. *AIAA J.* **3**, 216–223.

DRITSCHEL, D. G. 1986 The nonlinear evolution of rotating configurations of uniform vorticity. *J. Fluid Mech.* **172**, 157–182.

DRITSCHEL, D. G. 1988 Strain-induced vortex stripping. In *Mathematical Aspects of Vortex Dynamics* (ed. R. E. Caflisch), pp. 107–119. SIAM.

DUCK, P. W. & KHORRAMI, M. R. 1991 On the effects of viscosity on the stability of a trailing-line vortex. *ICASE Rep.* 91-6.

HAYASHI, Y.-Y. & YOUNG, W. R. 1987 Stable and unstable shear modes of rotating parallel flows in shallow water. *J. Fluid Mech.* **184**, 477–504.

HOWARD, L. N. 1973 On the stability of compressible swirling flow. *Stud. Appl. Maths* **52**, 39–43.

HOWE, M. S. 1975 Contributions to the theory of aerodynamic sound, with application to excess jet noise and the theory of the flute. *J. Fluid Mech.* **71**, 625–673.

HULTGREN, L. S. 1988 Stability of swirling gas flows. *Phys. Fluids* **31**, 1872–1876.

INCE, E. L. 1926 *Ordinary Differential Equations.* Longmans, Green & Co. Ltd.

JAMESON, A., SCHMIDT, W. & TURKEL, E. 1981 Numerical solutions of the Euler equations by finite volume methods using Runge–Kutta time-stepping schemes. *AIAA Paper* 81-1259.

KELVIN, LORD 1880 Vibrations of a columnar vortex. *Lond. Edinb. Dubl. Phil. Mag.* **10** (5), 155–168.

KHORRAMI, M. R. 1991 On the viscous modes of instability of a trailing line vortex. *J. Fluid Mech.* **225**, 197–212.

KLYATSKIY, V. I. 1966 Emission of sound by a system of vortices. *Izv. Akad. Nauk SSSR Mech. Zhid Gaza* No. 6, 87–92.

KOP'EV, V. F. & LEONT'EV, E. A. 1983 Acoustic instability of an axial vortex. *Sov. Phys. Acoust.* **29**, 111–115.

KOP'EV, V. F. & LEONT'EV, E. A. 1988 Acoustic instability of planar vortex flows with circular streamlines. *Sov. Phys. Acoust.* **34**, 276–278.

LAMB, H. 1932 *Hydrodynamics,* 6th edn. Cambridge University Press.

LELE, S. K. 1992 Compact finite difference schemes with spectral-like resolution. *J. Comput. Phys.* **103**, 16–42.

LIEPMANN, H. W. & ROSHKO, A. 1957 *Elements of Gasdynamics.* John Wiley and Sons.

LIGHTHILL, M. J. 1952 On sound generated aerodynamically. *Proc. R. Soc. Lond.* A **211**, 564–587.

LOVE, A. E. H. 1893 On the stability of certain vortex motions. *Proc. Lond. Math. Soc.* **35**, 18–42.

MANDELLA, M. 1987 Experimental and analytical studies of compressible vortices. PhD dissertation, Stanford University.

MITCHELL, B. E., LELE, S. K. & MOIN, P. 1992 Direct computation of the sound from a compressible co-rotating vortex pair. *AIAA Paper* 92-0374.

MOORE, D. W. & SAFFMAN, P. G. 1973 Axial flow in laminar trailing vortices. *Proc. R. Soc. Lond.* A **333**, 491–508.

MÜLLER, E. A. & OBERMEIER, F. 1967 The spinning vortices as a source of sound. Fluid Dynamics of Rotor and Fan Supported Aircraft at Subsonic Speeds. *AGARD Conf. Proc.* 22.

PULLIAM, T. H. 1986*a* *Efficient Solution Methods for the Navier–Stokes Equations.* Lecture Notes For The Von Karman Institute For Fluid Dynamics Lecture Series: Numerical Techniques For Viscous Flow Computation In Turbomachinery Bladings.

PULLIAM, T. H. 1986*b* Artificial dissipation models for the Euler equations. *AIAA J.* **24**, 1931–1940.

RIPA, P. 1987 On the stability of elliptical vortex solutions of the shallow water equations. *J. Fluid Mech.* **183**, 343–363.

SANDHAM, N. D. 1989 A numerical investigation of the compressible mixing layer. PhD dissertation, Stanford University.

SOZOU, C. 1969 *a* Symmetrical normal modes in a Rankine vortex. *J. Acoust. Soc. Am.* **46**, 814–818.

SOZOU, C. 1969*b* Adiabatic transverse modes in a uniformly rotating fluid. *J. Fluid Mech.* **36**, 605–612.

SOZOU, C. 1987*a* Adiabatic perturbations in an unbounded Rankine vortex. *Proc. R. Soc. Lond.* A **411**, 207–224.

SOZOU, C. 1987*b* New solutions representing adiabatic transverse waves in a Rankine vortex. *Proc. R. Soc. Lond.* A **413**, 225–234.

SOZOU, C. & SWITHENBANK, J. 1969 Adiabatic transverse waves in a rotating fluid. *J. Fluid Mech.* **38**, 657–671.

SOZOU, C. & WILKINSON, L. C. 1989 Fast rotating polytropic gas: some new wave solution for a classical problem. *Proc. R. Soc. Lond.* A **422**, 329–342.

STEGER, J. L. & WARMING, R. F. 1981 Flux vector splitting of the inviscid gasdynamic equations with application to finite-difference methods. *J. Comput. Phys.* **40**, 263–293.

THOMPSON, K. W. 1987 Time dependent boundary conditions for hyperbolic systems. *J. Comput. Phys.* **68**, 1–24.

WILLIAMS, J. S. 1992 Nonlinear problems in vortex sound. PhD dissertation, University of Leeds.

WRAY, A. A. 1986 Very low storage time-advancement schemes. Internal Report, NASA Ames Research Center, Moffett Field, Calif.

YING, S. X. 1986 Three-dimensional implicit approximately factored schemes for the equations of gasdynamics. PhD dissertation, Stanford University.

ZEITLIN, V. 1991 On the backreaction of acoustic radiation for distributed two-dimensional vortex structures. *Phys. Fluids* A **3**, 1677–1680.